

Single Crystal Growth, Crystallography, Magnetic Susceptibility, Heat Capacity, and Thermal Expansion of the Antiferromagnetic $S = 1$ Chain Compound CaV_2O_4

A. Niazi,^{1,*} S. L. Bud'ko,^{1,2} D. L. Schlagel,³ J. Q. Yan,³ T. A. Lograsso,³ A. Kreyssig,^{1,2} S. Das,^{1,2} S. Nandi,^{1,2} A. I. Goldman,^{1,2} A. Honecker,⁴ R. W. McCallum,³ M. Reehuis,^{5,6} O. Pieper,^{7,8} B. Lake,^{7,8} and D. C. Johnston^{1,2}

¹Ames Laboratory, Ames, Iowa 50011, USA

²Department of Physics and Astronomy, Iowa State University, Ames, Iowa 50011, USA

³Materials and Engineering Physics Program, Ames Laboratory, Ames, Iowa 50011, USA

⁴Institut für Theoretische Physik, Universität Göttingen, D-37077 Göttingen, Germany

⁵Helmholtz-Zentrum Berlin für Materialien und Energie (HZB), Glienicker Straße 100, 14109 Berlin, Germany

⁶Max-Planck-Institut für Festkörperforschung, Heisenbergstr. 1, D-70569 Stuttgart, Germany

⁷Hahn-Meitner-Institut, Glienicker Str. 100, D-14109 Berlin, Germany

⁸Institut für Festkörperphysik, Technische Universität Berlin, Hardenbergstr. 36, D-10623 Berlin, Germany

(Dated: October 31, 2018)

The compound CaV_2O_4 contains V^{+3} cations with spin $S = 1$ and has an orthorhombic structure at room temperature containing zigzag chains of V atoms running along the c -axis. We have grown single crystals of CaV_2O_4 and report crystallography, static magnetization, magnetic susceptibility χ , ac magnetic susceptibility, heat capacity C_p , and thermal expansion measurements in the temperature T range of 1.8–350 K on the single crystals and on polycrystalline samples. An orthorhombic to monoclinic structural distortion and a long-range antiferromagnetic (AF) transition were found at sample-dependent temperatures $T_S \approx 108$ –145 K and $T_N \approx 51$ –76 K, respectively. In two annealed single crystals, another transition was found at ≈ 200 K. In one of the crystals, this transition is mostly due to V_2O_3 impurity phase that grows coherently in the crystals during annealing. However, in the other crystal the origin of this transition at 200 K is unknown. The $\chi(T)$ shows a broad maximum at ≈ 300 K associated with short-range AF ordering and the anisotropy of χ above T_N is small. The anisotropic $\chi(T \rightarrow 0)$ data below T_N show that the (average) easy axis of the AF magnetic structure is the b -axis. The $C_p(T)$ data indicate strong short-range AF ordering above T_N , consistent with the $\chi(T)$ data. We fitted our χ data by a J_1 - J_2 $S = 1$ Heisenberg chain model, where $J_1(J_2)$ is the (next)-nearest-neighbor exchange interaction. We find $J_1 \approx 230$ K, and surprisingly, $J_2/J_1 \approx 0$ (or $J_1/J_2 \approx 0$). The interaction J_\perp between these $S = 1$ chains leading to long-range AF ordering at T_N is estimated to be $J_\perp/J_1 \gtrsim 0.04$.

PACS numbers: 75.40.Cx, 75.50.Ee, 75.10.Pq, 81.10.Fq

I. INTRODUCTION

Low-dimensional frustrated spin systems have rich phase diagrams arising from a complex interplay of thermal and quantum fluctuations and competing magnetic interactions at low temperatures. While spin $S = 1/2$ antiferromagnetic (AF) chains¹ and odd-leg ladders^{2,3} have gapless magnetic excitations, $S = 1$ chains and $S = 1/2$ even-leg ladders with nearest-neighbor (NN, J_1) interactions exhibit a finite energy gap between the ground state and the lowest excited magnetic states. However, numerical calculations have shown that the influence of frustrating next-nearest-neighbor (NNN, J_2) interactions play a significant role and depending on the J_2/J_1 ratio, can lead to incommensurate helical spin structures which may be gapped or gapless.^{4,5,6,7,8} Such a system is described by the XXZ Hamiltonian⁴

$$\mathcal{H} = \sum_{\rho=1}^2 J_\rho \sum_l (S_l^x S_{l+\rho}^x + S_l^y S_{l+\rho}^y + \lambda S_l^z S_{l+\rho}^z), \quad (1)$$

where \mathbf{S}_l is the spin operator at the l th site, J_ρ is the AF interaction between the NN ($\rho = 1$) and NNN ($\rho = 2$) spin pairs, and λ is the exchange anisotropy. For $j \equiv J_2/J_1 > 1/4$, the classical AF chain exhibits incom-

mensurate helical long-range ordering described by the wave vector $q = \arccos[-1/(4j)]$ and a finite *vector chirality* $\vec{\kappa} = \mathbf{S}_i \times \mathbf{S}_{i+1}$ which describes the sense of rotation (left or right handed) of the spins along the helix. In the large- j , small- λ limit of the $S = 1$ chain, one finds a corresponding phase⁵ where spin correlations decay, as required for a one-dimensional system, although only algebraically, but chirality is still long-range ordered. This phase is called the *chiral gapless phase* and is seen to exist for all spin quantum numbers S .^{6,7} For smaller j , a *chiral gapped phase* is observed in the $S = 1$ chain,⁵ with chiral long-range order and exponentially decaying spin correlations.

The above chiral phases are ground state phases of a spin system. In a related prediction, Villain suggested three decades ago that a long-range ordered vector chiral phase can exist above the Néel temperature T_N of a quasi-one-dimensional spin chain system showing helical magnetic ordering below T_N .⁹ This chiral phase would have a transition temperature $T_0 > T_N$ that could be detected using heat capacity measurements.⁹

The compound CaV_2O_4 , containing crystallographic V^{+3} spin $S = 1$ zigzag chains, has been suggested as a model experimental system to study the above chiral gapless phase.^{10,11} CaV_2O_4 crystallizes in the CaFe_2O_4

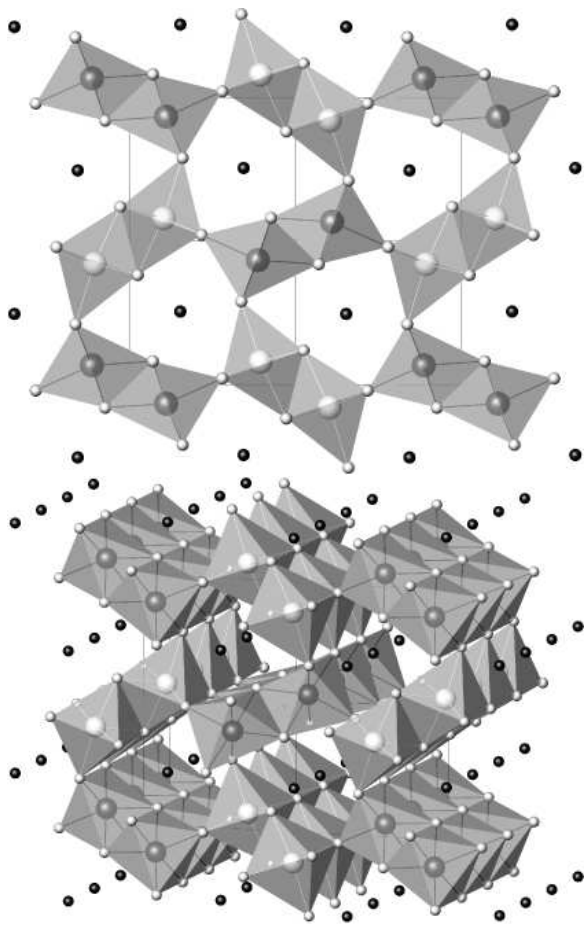


FIG. 1: End-on (top) and inclined (bottom) views along the c -axis of the CaV_2O_4 structure showing the V zigzag chains with the V atoms in distorted edge- and corner-sharing octahedral coordination by oxygen.

structure at room temperature^{12,13} with the orthorhombic space group $Pnam$ and with all the atoms in distinct Wyckoff positions $4(c)$ ($x, y, 1/4$) in the unit cell. As shown in Figs. 1 and 2, two zigzag chains of distorted edge- and corner-sharing VO_6 octahedra occur within the unit cell and run parallel to the c -axis, with the Ca ions situated in tunnels between the chains. Two sets of crystallographically inequivalent V atoms occupy the two zigzag chains, respectively. The VO_6 octahedra within a zigzag chain share corners with the octahedra in the adjacent zigzag chain. Within each zigzag chain, in order to be consistent with our theoretical modeling later in Sec. IV of the paper, the nearest neighbors are *defined* to be those on different legs of the zigzag chain where the NN V-V distance is 3.07 \AA . The NNN V-V distance (3.01 \AA) is *defined* to be along a leg of the zigzag chain. The similarity between these two distances in CaV_2O_4 suggests that $J_1 \approx J_2$, which would result in geometrically frustrated AF interactions in this insulating low-dimensional system.^{10,11}

Previous studies on polycrystalline samples of CaV_2O_4 have offered contrasting views on the nature of the mag-

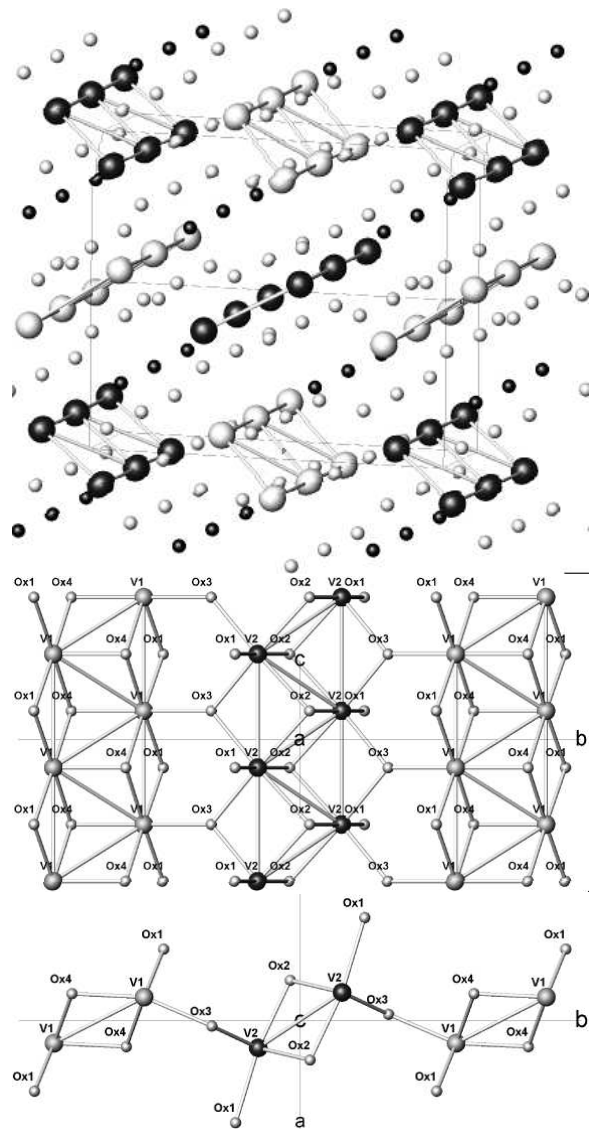


FIG. 2: Top panel: the skeletal structure of CaV_2O_4 showing the zigzag V-V chains. The large spheres represent V atoms, the small dark spheres Ca atoms, and the small light spheres O atoms. Middle and bottom panels: cross-sections of the b - c and a - b planes, with the V and O atoms labeled as described in Table II. The Ca atoms have been omitted for clarity.

netic ground state. Magnetic neutron diffraction measurements on CaV_2O_4 (Ref. 13) gave clear evidence for the presence of long-range antiferromagnetic ordering at 4.2 K (the temperature dependence was not studied, and the Néel temperature was not determined). A doubled magnetic unit cell along the b and c directions was found with AF propagation vector $(0 \frac{1}{2} \frac{1}{2})$ and three collinear AF models with the V ordered moments parallel to the b -axis were considered. Interestingly, the ordered moment was found to be $1.06(6) \mu_B/(\text{V atom})$, where μ_B is the Bohr magneton. This value is a factor of two smaller than the value $gS\mu_B = 2.0 \mu_B/(\text{V atom})$ expected for a spin $S = 1$ with spectroscopic splitting factor (g -factor)

$g = 2$. Magnetic susceptibility measurements^{10,11} showed a broad maximum at ~ 250 K, indicating the onset of strong short-range AF ordering in a low-dimensional spin system upon cooling. The data also showed a finite value at the lowest temperatures, indicating that an energy gap for spin excitations did not occur, consistent with the neutron diffraction measurements. However, these magnetic susceptibility data also showed a bifurcation below ~ 20 K between low field (100 Oe) zero-field-cooled and field-cooled measurements that was suggestive of a spin-glass-like freezing rather than long-range AF ordering. ^{51}V nuclear magnetic resonance (NMR) measurements^{10,11} showed a nuclear spin-lattice relaxation rate $1/T_1 \propto T$ at low temperatures from 2 K to 30 K, of unknown origin, but again indicating lack of an energy gap for magnetic excitations. The authors^{10,11} proposed a *chiral gapless ordered* phase at low temperatures in accordance with theoretical predictions for a $S = 1$ frustrated XY or XXZ chain. The chiral phase implies a helical spin arrangement in contrast to the collinear spin models proposed¹³ in the neutron diffraction study. Furthermore, the observation of a ^{51}V nuclear resonance at the normal ^{51}V Larmor frequency^{10,11} at temperatures at and below 4 K is not consistent with the long-range antiferromagnetic ordering found at 4 K from the neutron diffraction measurements,¹³ since such ordering produces a very large static local magnetic field of order 20 T at the positions of the V nuclei.

In order to resolve the above inconsistencies regarding the magnetic ground state of CaV_2O_4 and to search for interesting physics in this system associated with possible geometric frustration within the zigzag spin chains, we have for the first time (to our knowledge) grown single crystals of this compound, and report herein crystal structure, static magnetization and magnetic susceptibility $\chi(T)$, ac magnetic susceptibility $\chi_{\text{ac}}(T)$, heat capacity $C_p(T)$, and anisotropic linear thermal expansion $\alpha_i(T)$ ($i = x, y, z$) measurements over the temperature T range 1.8 to 350 K on polycrystalline and single crystal samples. Our $\chi(T)$ and $\chi_{\text{ac}}(T)$ measurements do not show any signature of a spin-glass transition around 20 K as previously reported.^{10,11} We instead observe long-range antiferromagnetic (AF) ordering at sample-dependent Néel temperatures $T_N \approx 51\text{--}76$ K.

We have recently reported elsewhere the results of ^{17}O NMR measurements on a polycrystalline sample of CaV_2O_4 and find a clear signature of AF ordering at $T_N \approx 78$ K.¹⁴ We find no evidence of a ^{51}V NMR signal at the normal Larmor frequency at temperatures between 4 K and 300 K, in conflict with the above previous ^{51}V NMR studies which did find such a resonance.^{10,11} In single crystals, at temperatures below 45 K we do find a *zero-field* ^{51}V NMR signal where the ^{51}V nuclei resonate in the static component of the local magnetic field generated by the long-range AF order below $T_N \approx 70$ K.¹⁴ The ordered moment at 4.2 K in the crystals was estimated from the zero-field ^{51}V NMR measurements to be $1.3(3) \mu_B/(\text{V atom})$, somewhat larger than but still

consistent with the value $1.06(6) \mu_B/(\text{V atom})$ from the above neutron diffraction measurements.¹³ An energy gap Δ for antiferromagnetic spin wave excitations was found with a value $\Delta/k_B = 80(20)$ K in the temperature range 4–45 K, where k_B is Boltzmann's constant. This energy gap was proposed to arise from single-ion anisotropy associated with the $S = 1 \text{V}^{+3}$ ion. A model for the antiferromagnetic structure at 4 K was formulated in which the magnetic structure consists of two substructures, each of which exhibits collinear antiferromagnetic order, but where the easy axes of the two substructures are at an angle of $19(1)^\circ$ with respect to each other. The *average* easy axis direction is along the b -axis, consistent with our magnetic susceptibility measurements to be presented here, and with the easy-axis direction proposed in the earlier neutron diffraction measurements.¹³ Our magnetic neutron diffraction studies of the antiferromagnetic structure of CaV_2O_4 single crystals are qualitatively consistent with the NMR analyses; these results together with high-temperature ($T \leq 1000$ K) magnetic susceptibility measurements and their analysis are presented elsewhere.¹⁵

We also find that CaV_2O_4 exhibits a weak orthorhombic to monoclinic structural distortion upon cooling below a sample-dependent temperature $T_S = 108\text{--}147$ K, discovered from our neutron and x-ray diffraction measurements to be reported in detail elsewhere.¹⁶ In our two *annealed single crystals* only, anomalies in the heat capacity and thermal expansion are also found at $T_{S1} \approx 200$ K. From high-energy x-ray diffraction measurements reported here, we find that in one of the crystals the anomaly is most likely primarily due to the metal-insulator and structural transitions in V_2O_3 impurity phase that grows coherently in the crystal when it is annealed. In the other crystal, we still find a small anomaly in the heat capacity at T_{S1} but where the transition in the V_2O_3 impurity phase is at much lower temperature. Hence we infer that there is an intrinsic transition in our two annealed CaV_2O_4 crystals at T_{S1} with an unknown origin. We speculate that this transition may be the long-sought chiral ordering transition envisioned by Villain⁹ that was mentioned above.

From our inelastic neutron scattering results to be published elsewhere,¹⁷ we know that the magnetic character of CaV_2O_4 is quasi-one-dimensional as might be inferred from the crystal structure. The largest dispersion of the magnetic excitations is along the zigzag chains, which is along the orthorhombic c -axis direction, with the dispersion along the two perpendicular directions roughly a factor of four smaller. This indicates that the exchange interactions perpendicular to the zigzag chains are roughly an order of magnitude smaller than within a chain. We therefore analyze the magnetic susceptibility results here in terms of theory for the $S = 1 J_1\text{--}J_2$ linear Heisenberg chain, where $J_1(J_2)$ is the (next-)nearest-neighbor interaction along the chain. With respect to the interactions, this chain is topologically the same as a zigzag chain where J_1 is the nearest-neighbor interaction between

spins in the two different legs of the zigzag chain and J_2 is the nearest-neighbor interaction between spins within the same leg. We utilize exact diagonalization to calculate the magnetic susceptibility and magnetic heat capacity for chains containing up to 14 spins $S = 1$, and quantum Monte Carlo simulations of the magnetic susceptibility and heat capacity for chains of 30 and 60 spins. We obtain estimates of J_1 , J_2/J_1 , the temperature-independent orbital susceptibility χ_0 , and the zero-temperature spin susceptibilities in CaV_2O_4 from comparison of the theory with the experimental $\chi(T)$ data near room temperature. Remarkably, we find that one of the two exchange constants is very small compared to the other near room temperature, as opposed to $J_1/J_2 \approx 1$ that is expected from the crystal structure. Thus, with respect to the magnetic interactions, the zigzag crystallographic chain compound acts instead like a linear $S = 1$ Haldane spin chain compound. In Ref. 15, we propose that partial orbital ordering is responsible for this unexpected result, and suggest a particular orbital ordering configuration. In Ref. 15, we also deduce that below $T_S \sim 150$ K, the monoclinic distortion results in a change in the orbital ordering that in turn changes the nature of the spin interactions from those of a Haldane chain to those of a $S = 1$ two-leg spin ladder. Here we also compare the theory for the magnetic heat capacity with the results of our heat capacity experiments. We estimate the coupling J_\perp between these chains that leads to the long-range AF order at T_N .

The remainder of this paper is organized as follows. The synthesis and structural studies are presented in Sec. II. The magnetization, magnetic susceptibility, heat capacity and thermal expansion measurements are presented in Sec. III. In Sec. IV we consider the origin of the heat capacity and thermal expansion anomalies at $T_{S1} \approx 200$ K. We then analyze the $\chi(T)$ data in terms of the predictions of exact diagonalization calculations and quantum Monte Carlo simulations to obtain J_1 , J_2/J_1 and χ_0 . Using the same J_1 and J_2/J_1 parameters, we compare the predicted behavior of the magnetic heat capacity with the experimentally observed heat capacity data. We also obtain an estimate of the interchain coupling J_\perp giving rise to long-range AF order at T_N . A summary of our results is given in Sec. V.

II. SYNTHESIS, SINGLE CRYSTAL GROWTH, AND CRYSTAL STRUCTURE OF CaV_2O_4

A. Synthesis and Crystal Growth

Polycrystalline CaV_2O_4 was synthesized via solid state reaction by first mixing V_2O_3 (99.995%, MV Labs) with CaCO_3 (99.995%, Aithaca Chemicals) or CaO obtained by calcining the CaCO_3 at 1100 °C. The chemicals were ground inside a He glove-box, pressed and sintered at 1200 °C for 96 hours in flowing 4.5% H_2 -He, as well as in sealed quartz tubes when using CaO , with interme-

mediate grindings. Phase purity was confirmed by powder x-ray diffraction (XRD) patterns obtained using a Rigaku Geigerflex diffractometer with $\text{Cu K}\alpha$ radiation in the angular range $2\theta = 10\text{--}90^\circ$ accumulated for 5 s per 0.02° step. Thermogravimetric analysis (TGA) at 800 °C using a Perkin Elmer TGA 7 was used to check the oxygen content by oxidizing the sample to CaV_2O_6 . A typical oxygen content of $\text{CaV}_2\text{O}_{3.98\pm 0.05}$ was determined, consistent with the initial stoichiometric composition CaV_2O_4 .

CaV_2O_4 was found to melt congruently in an Ar arc furnace with negligible mass loss by evaporation. Therefore crystal growth was attempted by pulling a crystal from the melt in a triarc furnace (99.995% Ar) using a tungsten seed rod.¹⁸ The triarc furnace was custom made for us by Materials Research Furnaces, Inc. Using 15–20 g premelted buttons of CaV_2O_4 , pulling rates of 0.2–0.5 mm/min were used to grow ingots of about 3–6 mm diameter and 3.0–4.7 cm length. The length of the ingot was limited by contraction of the molten region as power was lowered to control the crystal diameter. Obtaining a single grain was difficult because small fluctuations in the arcs coupled with high mobility of the CaV_2O_4 melt easily caused nucleation of new grains. Out of multiple growth runs, a reasonably large single grain section could be cut out of one of the ingots. The as-grown ingot from the triarc furnace and a single crystal isolated and aligned from it are shown in Figs. 3(a) and (b), respectively. Due to the tendency for multiple nucleations in the triarc furnace, an optical floating zone (OFZ) furnace was subsequently used for crystal growth.¹⁸ Growth rates and Ar atmosphere flow rates were optimized to successfully grow large crystals of 4–5 mm diameter and 4–5 cm length starting from sintered polycrystalline rods with masses of 8–10 g. An as-grown rod from the OFZ furnace is shown in Fig. 3(c).

Powder XRD of crushed sections from the triarc grown ingots as well as from the OFZ grown crystals showed single phase CaV_2O_4 . Laue x-ray diffraction patterns of a single-grain section confirmed its single-crystalline character and the crystal was found to grow approximately along its crystallographic c -axis. The crystals were oriented and cut to obtain faces aligned perpendicular to the principal axes. They were measured as grown (only for the triarc grown crystals) as well as after annealing in flowing 5% H_2 -He gas at 1200 °C for up to 96 hours.

B. Powder and Single Crystal X-ray and Neutron Diffraction Measurements

Rietveld refinements of the powder x-ray diffraction data obtained at room temperature were carried out using the program DBWS9807a.¹⁹ The refined powder XRD patterns from a polycrystalline sample and crushed pieces of the triarc and optical floating zone grown crystals are shown in Fig. 4 and the refinement results are presented in Tables I, II, and III. The XRD of the powdered

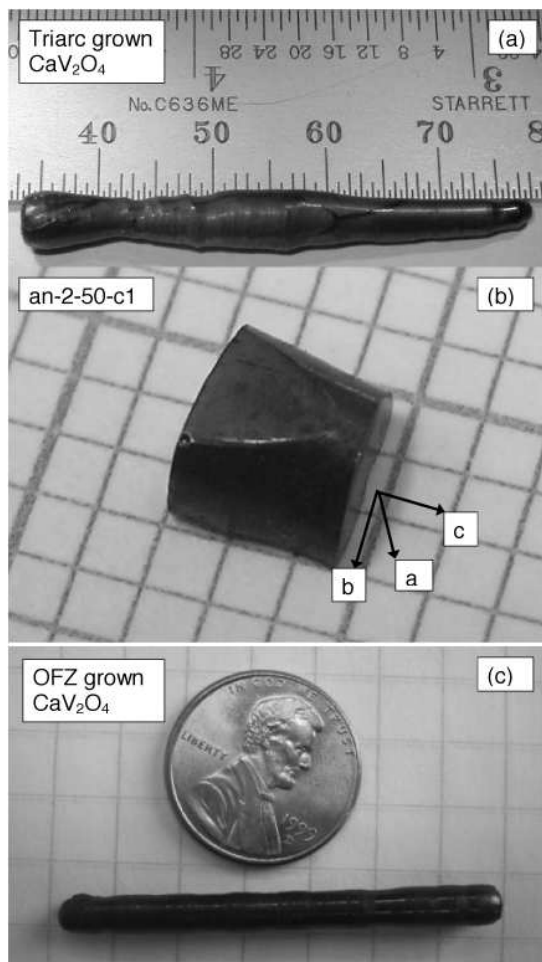


FIG. 3: Single crystals of CaV_2O_4 grown using (a), (b) a triarc furnace (a numbered division on the scale is 1 mm) and (c) an optical floating zone furnace (compared with a U.S. penny).

annealed single crystal samples showed a trace amount (~ 1 – 2 mol%) of V_2O_3 . It is curious that no trace was found of V_2O_3 impurity phase in the as-grown crystals, and that this impurity phase only formed after annealing the crystals. From the refinement results, the structural parameters remain relatively unchanged between polycrystalline samples prepared by the solid state route and both as-grown and annealed single crystals grown from the melt.

Single-crystal neutron diffraction data were collected on the four-circle diffractometer E5 at the BERII reactor of the Helmholtz-Zentrum Berlin, Germany. A pyrolytic graphite monochromator was used to select the neutron wavelength $\lambda = 2.36$ Å. Second order contamination was suppressed below 10^{-3} of first order by a pyrolytic graphite filter. Bragg reflections of CaV_2O_4 were measured with a two-dimensional position sensitive ^3He detector, 90×90 mm² in area. The sample was mounted in a closed-cycle refrigerator, where the temperature was controlled between 290 K and 6 K. A struc-

tural phase transition at temperature T_S from the high temperature orthorhombic structure to a low temperature monoclinic structure was found.¹⁶ This transition is reflected in Fig. 5 by a sudden change in the $(0\ 3\ 1)$ Bragg peak intensity which occurs at a temperature $T_S \approx 112$ K for the as-grown triarc crystal, and ≈ 141 K and ≈ 147 K for the annealed triarc and OFZ-grown crystals, respectively. Due to twinning the orthorhombic $(0\ 3\ 1)$ reflection splits below the structural phase transition into the $(0\ 3\ 1)$ and $(0\ \bar{3}\ 1)$ monoclinic reflections. The total integrated intensity at this position increases at T_S because of the increased mosaic which results in a reduction of the extinction effect. The peak in the intensity at 105 K for the as-grown triarc crystal is an experimental artifact due to multiple scattering. The lattice parameters of the low temperature monoclinic phase differ very little from the orthorhombic phase and the monoclinic angle $\alpha \approx 89.3^\circ$ is close to 90° . This result and the smoothly varying signatures in the thermodynamic properties suggest that the structural transition is of second order and involves a small distortion of the orthorhombic structure. Full details of the neutron and x-ray diffraction structural measurements and results will be presented elsewhere.¹⁶

A higher temperature anomaly in the temperature dependence of the lattice parameters of a powder sample was observed by x-ray diffraction over a temperature range of 175–200 K. This transition with $T_{S1} \approx 200$ K was also observed in the magnetic susceptibility, thermal expansion, and heat capacity measurements of two *annealed single crystals* as described in Sec. III below. In the next section we investigate whether there is a structural aspect to this phase transition.

C. High Energy X-ray Diffraction Measurements on Annealed CaV_2O_4 Single Crystals

In order to unambiguously determine the crystallographic structure of CaV_2O_4 at various temperatures, to characterize structural phase transitions, and to check the crystal perfection, high-energy x-ray diffraction measurements ($E = 99.43$ keV) using an area detector were performed on two annealed single crystals at the Advanced Photon Source at Argonne National Laboratory. At this high energy, x-rays probe the bulk of a crystal rather than just the near-surface region and, by rocking the crystal about both the horizontal and vertical axes perpendicular to the incident x-ray beam, an extended range of a chosen reciprocal plane can be recorded.²⁰ For these measurements, a crystal was mounted on the cold-finger of a closed-cycle refrigerator surrounded by the heat shield and vacuum containment using Kapton windows to avoid extraneous reflections associated with Be or the aluminum housing. Two orientations of the crystal, with either the $[001]$ or $[100]$ direction parallel to the incident beam, were studied allowing the recording of the $(hk0)$ or $(0kl)$ reciprocal planes. For each data set, the horizontal angle, μ , was scanned over a range of

TABLE I: Structure parameters at room temperature for CaV_2O_4 forming in the CaFe_2O_4 structure, refined from powder XRD data. Space Group: $Pnam$ (#62); $Z = 4$; Atomic positions: $4(c)$, $(x, y, 1/4)$; Profile: Pseudo-Voigt. The overall isotropic thermal parameter B is defined within the temperature factor of the intensity as $e^{-2B \sin^2 \theta / \lambda^2}$.

Sample	Synthesis	a (Å)	b (Å)	c (Å)	B (Å ²)	R_{wp} (%)	R_{p} (%)
an-2-116	1200 °C solid state	9.2064(1)	10.6741(1)	3.0090(1)	2.33(4)	11.17	8.24
an-2-50	Triarc as grown	9.2241(11)	10.6976(13)	3.0046(4)	1.72(5)	12.05	9.27
an-2-50	Triarc annealed 1200 °C	9.2054(3)	10.6748(3)	3.0042(1)	1.58(5)	14.54	10.95
an-3-074	OFZ annealed 1200 °C	9.2089(2)	10.6774(3)	3.0067(1)	0.75(5)	17.46	12.77

TABLE II: Atomic positions $(x, y, 1/4)$ for CaV_2O_4 obtained by Rietveld refinement of powder XRD data at room temperature for four samples.

Sample Number	an-2-116	an-2-50-c1	an-2-50-c1	an-3-074
Synthesis	Solid State	Triarc	Triarc	OFZ
	(1200 °C)	(as grown)	(annealed) ^a	(annealed) ^a
	x, y	x, y	x, y	x, y
Ca	0.7550(3), 0.6545(2)	0.7562(4), 0.6536(3)	0.7542(4), 0.6544(3)	0.7536(4), 0.6550(3)
V1	0.4329(2), 0.6117(1)	0.4320(3), 0.6120(2)	0.4336(3), 0.6120(2)	0.4331(3), 0.6114(2)
V2	0.4202(2), 0.1040(1)	0.4204(3), 0.1041(2)	0.4200(3), 0.1043(2)	0.4209(3), 0.1043(2)
O1	0.2083(6), 0.1615(5)	0.2128(8), 0.1593(7)	0.2049(8), 0.1603(8)	0.2074(9), 0.1635(9)
O2	0.1176(5), 0.4744(5)	0.1157(7), 0.4745(8)	0.1144(7), 0.4756(8)	0.1181(9), 0.4738(9)
O3	0.5190(7), 0.7823(5)	0.5153(11), 0.7812(7)	0.5166(0), 0.7806(7)	0.5169(11), 0.7797(8)
O4	0.4203(6), 0.4270(5)	0.4207(8), 0.4282(7)	0.4244(8), 0.4325(7)	0.4280(9), 0.4251(9)

^aTwo-phase sample containing $\sim 1\%$ V_2O_3 as determined from Rietveld refinement.

TABLE III: Bond angles V–O–V and bond lengths V–V for CaV_2O_4 at room temperature refined from powder XRD data and calculated using Atoms for Windows, version 5.0. The V_1 –O and V_2 –O bond lengths varied from 1.92 Å to 2.08 Å. The accuracy of the bond angles calculated is $\pm 0.1^\circ$.

Sample Number	an-2-116	an-2-50-c1	an-2-50-c1	an-3-074
Synthesis	Sintered powder	Triarc	Triarc	Optical float zone
	(1200 °C)	(as grown)	(annealed)	(annealed)
V_1 – O_1 – V_1 (NN)(°)	93.9	92.9	95.0	93.7
V_1 – O_4 – V_1 (NN)(°)	93.6	93.0	94.4	96.6
V_1 – V_1 (NN)(Å)	3.009	3.005	3.004	3.004
V_1 – O_4 – V_1 (NNN)(°)	99.3	99.9	101.8	100.3
V_1 – V_1 (NNN)(Å)	3.078	3.094	3.077	3.071
V_2 – O_2 – V_2 (NN)(°)	93.1	93.0	93.7	92.5
V_2 – O_3 – V_2 (NN)(°)	96.8	95.6	95.6	97.5
V_2 – V_2 (NN)(Å)	3.009	3.005	3.004	3.004
V_2 – O_3 – V_2 (NNN)(°)	97.3	98.0	98.3	97.1
V_2 – V_2 (NNN)(Å)	3.058	3.062	3.062	3.055
V_1 – O_1 – V_2 (°) ^a	121.7	122.9	121.8	121.0
V_1 – V_2 (Å) ^a	3.583	3.581	3.582	3.589
V_1 – O_3 – V_2 (°) ^b	131.6	132.2	132.2	132.2
V_1 – V_2 (Å) ^b	3.647	3.652	3.652	3.643

^aInterchain angles and distances parallel to a -axis

^bInterchain angles and distances parallel to b -axis

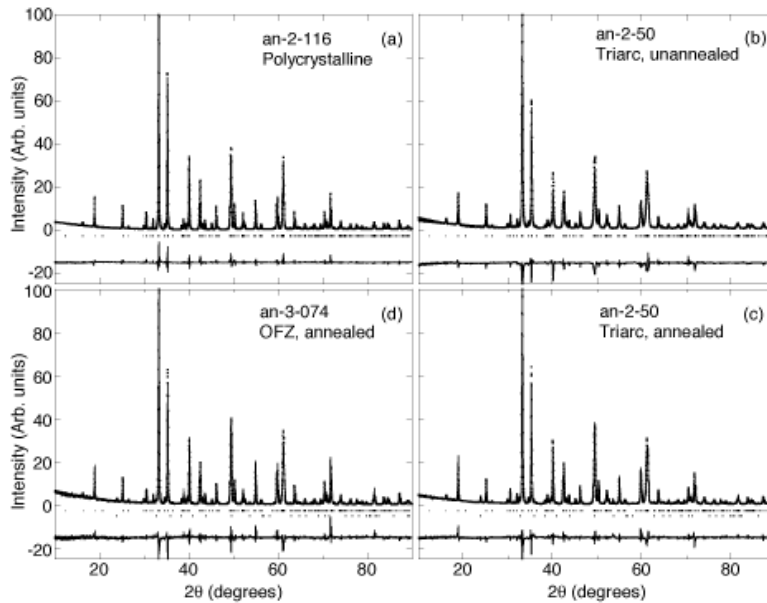


FIG. 4: Rietveld refinement of room temperature powder XRD data of CaV_2O_4 showing I_{obs} (+) I_{calc} (.), difference (—), and peak positions (|) for (a) a polycrystalline sample, (b) an as-grown triarc crystal, (c) an annealed triarc crystal, and (d) an annealed optical floating zone (OFZ) crystal. The annealed single crystal samples contain small XRD peaks from ~ 1 –2 mol% of V_2O_3 , shown as the lower sets of peak position markers.

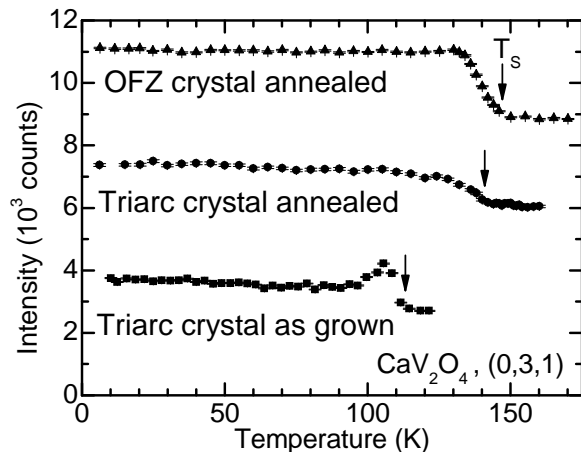


FIG. 5: Temperature variation of intensity of the (0 3 1) structural Bragg peak across the orthorhombic to monoclinic structural transition temperature (T_S) in single crystal samples of CaV_2O_4 measured by neutron diffraction. The (0 3 1) peak is present in both the orthorhombic and monoclinic phases.

± 2.4 deg for each value of the vertical angle, η , between ± 2.4 deg with a step size of 0.2 deg. The total exposure time for each frame was 338 sec. The x-ray diffraction patterns were recorded with different intensities of the incident beam that were selected by attenuation to increase the dynamic range to a total of 10^7 counts. A beam size of $0.3 \times 0.3 \text{ mm}^2$ was chosen to optimize the intensity/resolution condition and to allow probing different sections of the crystal by stepwise translations of the crystal in directions perpendicular to the incident

beam.

1. Annealed Triarc-Grown Crystal

Figure 6 shows the ($hk0$) diffraction plane of the annealed triarc sample an-2-50-c1 at 205 K. The reciprocal space image reveals well-defined diffraction spots that correspond to the “primary” CaV_2O_4 lattice, as well as spots that can be indexed to an impurity phase inclusion of V_2O_3 coherently oriented with respect to the CaV_2O_4 . No additional reflections were observed. Indeed, we find two coherent twins of V_2O_3 related by an inversion across a mirror plane of the CaV_2O_4 lattice as depicted by the black and white rectangles in the left panel of Fig. 6. By comparing the integrated intensities of reflections from the two phases, we estimate that V_2O_3 comprises a volume fraction of approximately 1–2 percent of the sample. This is in excellent agreement with the result of the x-ray diffraction analysis of the polycrystalline sample prepared from the same annealed crystal that was described above. The volume fraction of V_2O_3 varies only slightly in different parts of the crystal probed by scanning the x-ray beam over the crystal. This indicates that the inclusions of V_2O_3 are approximately equally distributed over the volume of the crystal.

Upon lowering the temperature of the crystal to 165 K, below $T_{S1} \sim 200$ K, we observe changes in the V_2O_3 structure consistent with the known first-order rhombohedral-to-monoclinic structural transition at 170 K (measured on heating).^{21,22} In particular, the upper left corners of both panels of Fig. 6 show enlarged

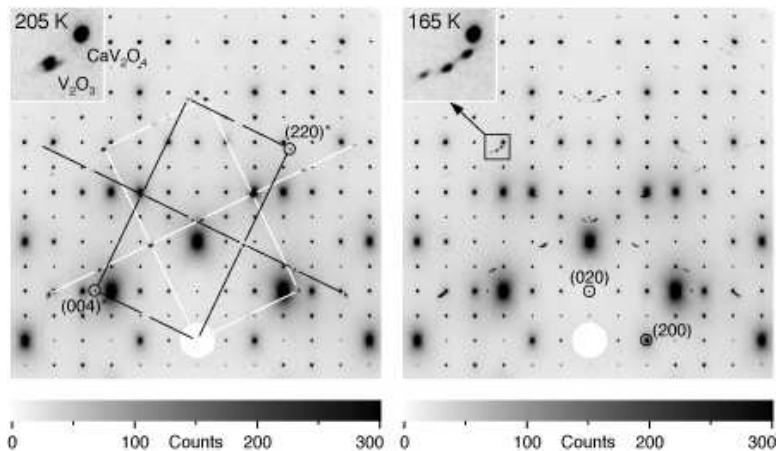


FIG. 6: High-energy x-ray diffraction patterns of the annealed triarc CaV_2O_4 crystal (an-2-50-c1), oriented with the $(hk0)$ plane coincident with the scattering plane at $T = 205$ K (left panel) and 165 K (right panel). The white circles in the lower center of each pattern depict the excluded areas around the primary x-ray beam direction. Several peaks corresponding to the main phase, CaV_2O_4 , as well as the coherently oriented second phase, V_2O_3 , are labeled by indices (hkl) and $(hkl)^*$, respectively. For V_2O_3 , the hexagonal Miller indices for the rhombohedral lattice are used. The insets of both panels display enlarged regions of the diffraction pattern to highlight the rhombohedral-to-monoclinic transition for V_2O_3 .

views of the region near the $(\bar{3}80)$ reflection from CaV_2O_4 and the (220) reflection (in hexagonal notation) for the rhombohedral lattice of V_2O_3 . Below T_{S1} the (220) reflection splits into three reflections in the monoclinic phase. The temperature dependence of this transition is displayed in Fig. 7. Here, we note that there is a finite range of coexistence between the rhombohedral and monoclinic phases of V_2O_3 (see the inset to Fig. 7) and the transition itself has a hysteresis of roughly 5–10 K.

Several points regarding Figs. 6 and 7 are relevant to our interpretation of the specific heat and thermal expansion measurements of the annealed triarc crystal (an-2-50-c1) to be presented below in Figs. 15 and 16, respectively. First, we note that over the temperature range encompassing the features at $T_{S1} \sim 200$ K, there is no apparent change in the diffraction pattern of CaV_2O_4 . These anomalies are instead strongly correlated with the rhombohedral-to-monoclinic transition in V_2O_3 . We further note that the temperature for this latter transition is somewhat higher than the accepted value of ≈ 170 K (determined on warming) found in the literature.^{21,23,24} This difference is, perhaps, due to the fact that the V_2O_3 and CaV_2O_4 lattices are coupled, as evidenced by the coherent orientation relationship between them, so that strains at the phase boundaries come into play and can raise the transition temperature.²⁵ In addition, it is reported^{23,24} that deviations of the stoichiometry from V_2O_3 can affect the transition temperature significantly.

We now turn our attention to changes in the diffraction pattern of CaV_2O_4 associated with anomalies in the heat capacity and thermal expansion measurements at temperatures $T_S \sim 150$ K in Figs. 15 and 16 below, respectively. The annealed triarc crystal (an-2-50-c1) was reoriented so that the CaV_2O_4 $(0kl)$ reciprocal lattice plane was set perpendicular to the incident beam. Fig-

ure 8 shows the diffraction patterns obtained at 205 K (above T_S) and 13 K (well below T_S). The strong reflections in Fig. 8 are associated with the main CaV_2O_4 lattice while the weaker diffraction peaks are, again, associated with the coherently oriented V_2O_3 second phase. At low temperatures, we observe a splitting of the main reflections that is the signature of the orthorhombic-to-monoclinic transition at T_S for the CaV_2O_4 lattice. The splitting of reflections associated with the transition at T_{S1} for V_2O_3 , in this reciprocal lattice plane, is not readily observed.

For the low-temperature monoclinic phase of CaV_2O_4 two possible space groups have been considered.¹⁶ The space groups $P 2_1/n 1 1$ and $P n 1 1$ can be separated by testing the occurrence or absence of $(0k0)$ reflections with k odd, respectively. The systematic absence of such reflections was proven by recording $(hk0)$ planes with varying conditions to evaluate the sporadic occurrence of these reflections by Rengers or multiple scattering. The space group $P 2_1/n 1 1$ is confirmed for the low-temperature phase of the studied CaV_2O_4 crystal. No changes in the diffraction pattern were observed related to the onset of antiferromagnetic order in CaV_2O_4 below $T_N = 69$ K.

The details of the orthorhombic-to-monoclinic transition at T_S for CaV_2O_4 are shown in Fig. 9 where we plot the monoclinic distortion angle as a function of temperature. The monoclinic angle was determined from the splitting of the peaks along the \mathbf{b} -direction through the position of the $(04\bar{2})$ reflection. Below $T_S = 138(2)$ K, the monoclinic angle evolves continuously, consistent with a second order transition, and saturates at approximately 89.2 deg at low temperatures.

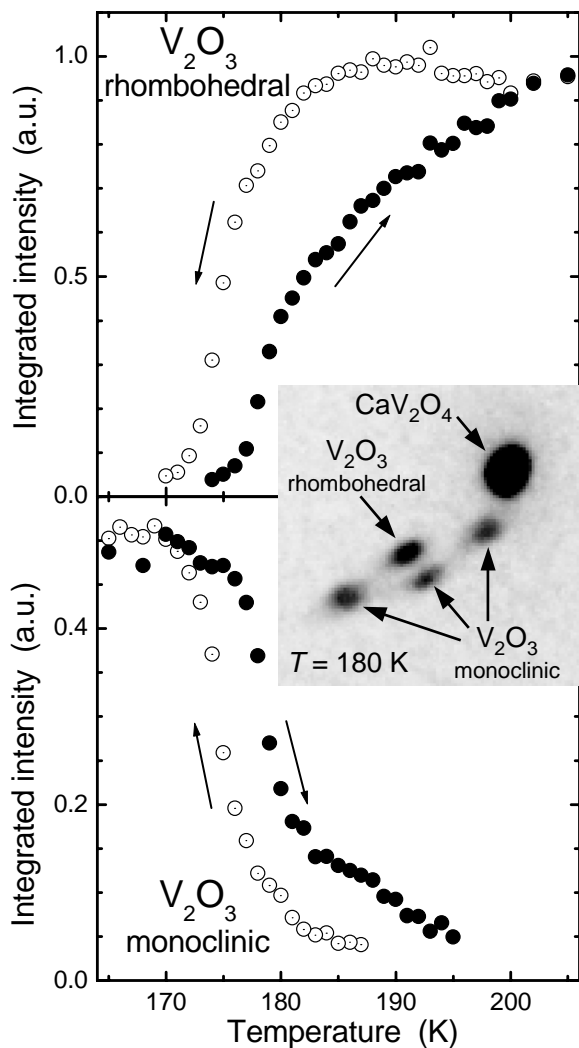


FIG. 7: Integrated intensity of selected reflections in the high-energy x-ray diffraction pattern related to the rhombohedral (top panel) and monoclinic (bottom panel) phases of V_2O_3 as a function of temperature for the annealed triarc crystal (an-2-50-c1). The direction of the temperature change is indicated by arrows. The inset displays the pattern observed at 180 K (with increasing temperature) for the (220) reflection from V_2O_3 in the coexistence temperature range. This region is the same as that displayed in the insets of Fig. 6.

2. Annealed OFZ-Grown Crystal

The annealed optical floating zone crystal (an-3-074 OFZ) shows a diffraction pattern similar to that of the annealed triarc-grown crystal (an-2-50-c1) in measurements of $(hk0)$ planes at room temperature. The observed V_2O_3 inclusions are again coherently oriented with respect to the CaV_2O_4 lattice. The intensities of the diffraction peaks related to V_2O_3 are similar to those in the annealed triarc crystal (an-2-50-c1) and also vary only slightly upon scanning different spots of the crystal which indicates a homogeneous distribution of the V_2O_3 inclusions with a similar volume fraction. However, the

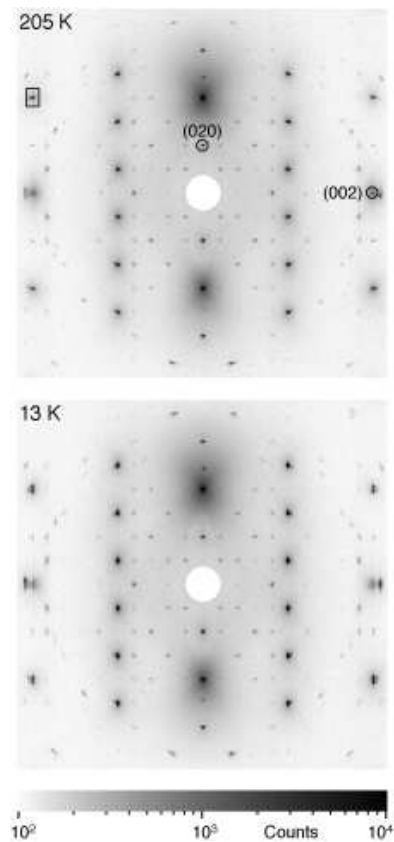


FIG. 8: High-energy x-ray diffraction patterns of the $(0kl)$ reciprocal lattice plane of CaV_2O_4 from the annealed triarc crystal (an-2-50-c1) at 205 K (top panel) and 13 K (bottom panel). The white circles in the center of the patterns depict the excluded areas around the primary x-ray beam direction. Most of the reflections related to CaV_2O_4 show intensities above 10^4 counts (see intensity scale). The (020) and (002) reflections of CaV_2O_4 are marked in the top panel. The area bounded by the black rectangle in the top panel depicts the region close to the orthorhombic $(04\bar{2})$ reflection of CaV_2O_4 , analyzed in Fig. 9.

temperature dependence of the diffraction pattern is different for the two crystals. Measurements taken on cooling show that in the annealed floating-zone crystal (an-3-074 OFZ), the shape and position of the peaks originating from V_2O_3 are stable from room temperature down to 130 K where the onset of the structural transition occurs. Around 120 K strong changes are observed similar to the observations around 180 K in the annealed triarc crystal (an-2-50-c1). Below 110 K, the transition to the low-temperature monoclinic structure of V_2O_3 is complete. Therefore, the temperature for the rhombohedral-to-monoclinic transition is reduced by ~ 60 K compared to the corresponding temperature in the annealed triarc crystal (an-2-50-c1).

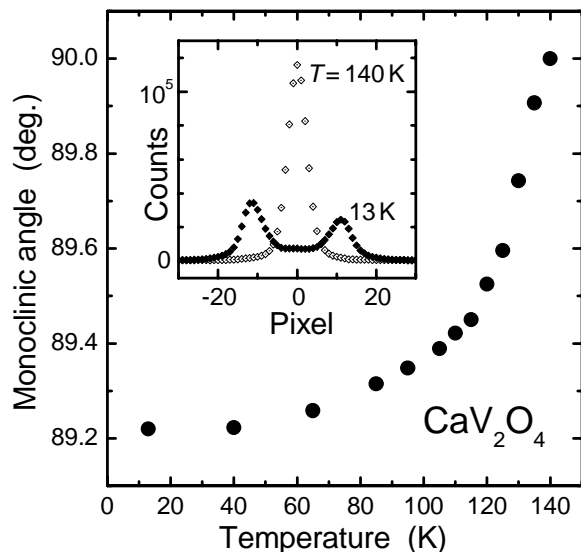


FIG. 9: Temperature dependence of the monoclinic angle in the low-temperature phase of CaV_2O_4 , extracted from diffraction data such as shown in the inset for temperatures of 140 K and 13 K. Such diffraction line scans were extracted from high-energy x-ray diffraction patterns by summing up the intensity perpendicular to the \mathbf{b} direction for the sector marked by the rectangle in the top panel of Fig. 8.

III. MAGNETIZATION, MAGNETIC SUSCEPTIBILITY, HEAT CAPACITY AND THERMAL EXPANSION MEASUREMENTS

In the following, we describe our results of magnetization, magnetic susceptibility, heat capacity, and thermal expansion measurements of both polycrystalline and single crystal samples. These and additional measurements consistently identify temperatures at which the antiferromagnetic transition (T_N), the orthorhombic-to-monoclinic structural transition (T_S) and the transition at ~ 200 K (T_{S1}) occur in these samples. In Table IV, we summarize these transition temperatures for the different samples obtained using the various measurements.

A. Magnetization and Magnetic Susceptibility Measurements

The static magnetic susceptibility versus temperature $\chi(T) \equiv M(T)/H$ of a polycrystalline sample as well as of the oriented crystals was measured using a Quantum Design MPMS SQUID magnetometer in a 1 T field from 1.8 K to 350 K, where M is the magnetization of the sample and H is the magnitude of the applied magnetic field. In addition, low field (100 Oe) zero-field-cooled and field-cooled (zfc, fc) measurements of $M(T)$ at fixed H were carried out from 1.8 K to 100 K. A Quantum Design MPMS ac SQUID magnetometer was used to measure the ac susceptibility $\chi_{ac}(T)$ of the annealed triarc grown crystal from 5 to 100 K in an ac field $H_{ac} = 1$ Oe and

TABLE IV: Antiferromagnetic ordering (Néel) temperature (T_N), high temperature orthorhombic to low-temperature monoclinic structural transition temperature (T_S), and the transition temperature at ~ 200 K (T_{S1}) observed by static magnetic susceptibility χ (peak of $d(\chi T)/dT$), heat capacity C_p (peak of ΔC_p), thermal expansion α [peak of $\alpha(T)$, except for T_{S1} where the onset of α slope change is used], powder synchrotron x-ray diffraction (XRD), single crystal neutron diffraction (ND), and single crystal high-energy x-ray diffraction (HEXRD) measurements for polycrystalline (powder) and single crystal CaV_2O_4 samples. The single crystals were grown using either a triarc furnace or an optical floating zone (OFZ) furnace.

Sample	Synthesis	Method	T_N (K)	T_S (K)	T_{S1} (K)
an-2-116	powder 1200 °C	χ	76	147	^a
		C_p	75	144	^a
		XRD	–	150	200
an-2-50	Triarc crystal as-grown	χ	51	108	^a
		C_p	51	108	^b
		ND	53	112	^b
an-2-50	Triarc crystal annealed 1200 °C	χ	68	133	195
		C_p	68	133	193
		α	68	136	198
		ND	69	141	^b
		HEXRD	–	138(2)	192(7) ^c
an-3-074	OFZ crystal annealed 1200 °C	χ	69	136	192
		C_p	71	132	191
		ND	69	147	^b

^aNo clear signature of a transition corresponding to T_{S1} was observed.

^bNot measured for this sample.

^cThe error bar reflects the hysteresis on warming and cooling.

frequency 10 Hz. The powder was contained in polycarbonate capsules mounted in clear plastic straws. Each crystal was glued to a small piece of clear plastic transparency sheet with GE 7031 varnish or Duco cement, which was then aligned inside the plastic straws with the a , b or c axis direction parallel to the external magnetic field. $M(H)$ isotherms were measured in fields up to $H = 5.5$ T at various temperatures.

The $\chi(T)$ in $H = 1$ T is plotted in Fig. 10 for a CaV_2O_4 polycrystalline sample and for aligned single crystals grown using a triarc furnace and using an optical floating zone (OFZ) furnace. The broad maximum in $\chi(T)$ around 300 K is characteristic of a low-dimensional spin system with dominant antiferromagnetic exchange interactions with magnitude of order 300 K. For the single crystal samples, clear evidence is seen for long-range antiferromagnetic ordering at Néel temperatures $T_N = 51$ to 69 K, depending on the sample. The easy axis of the antiferromagnetic ordering (with the lowest susceptibility as $T \rightarrow 0$) is seen to be the b -axis, perpendicular to the zigzag V chains. At temperatures above T_N , the susceptibility of the crystals is nearly isotropic, but with

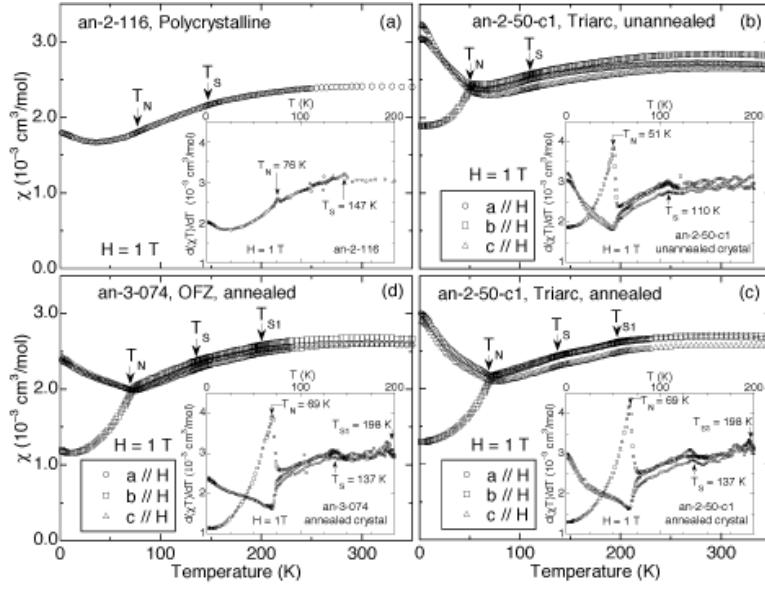


FIG. 10: Magnetic susceptibility χ versus temperature in a field of 1 T of CaV_2O_4 (a) polycrystalline sample, (b) as-grown triarc-grown single crystal, (c) annealed triarc-grown single crystal, and (d) annealed OFZ-grown single crystal. The axes (a , b , or c) along which the measurements were carried out are as indicated. The insets show $d(\chi T)/dT$ versus T to highlight the transition temperatures. The oscillatory behavior of $d(\chi T)/dT$ at the higher temperatures, most pronounced in the inset in (b), is an artifact generated by the SQUID magnetometer.

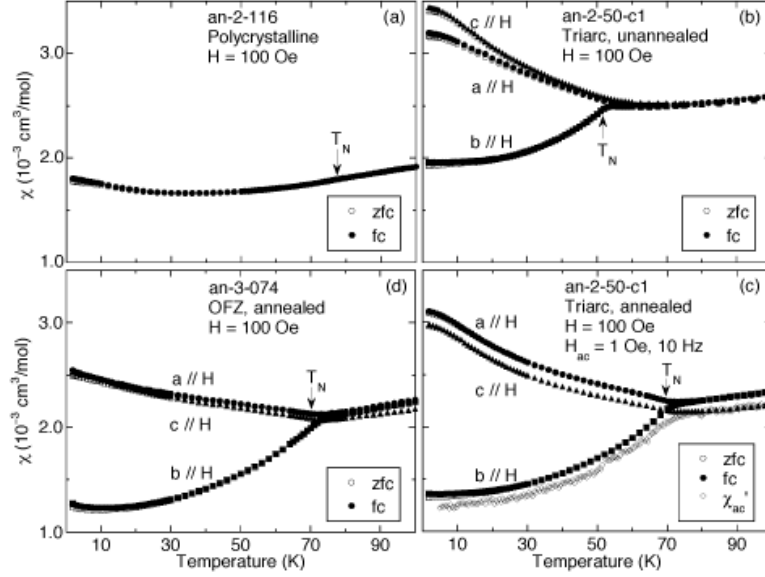


FIG. 11: Zero-field-cooled and field-cooled susceptibility of CaV_2O_4 in a field of 100 Oe measured on (a) polycrystalline powder, (b) unannealed triarc grown single crystal (c) annealed triarc grown single crystal, and (d) annealed OFZ grown single crystal. Part (c) also shows the ac-susceptibility $\chi'_{ac}(T)$ along the easy b -axis of the annealed crystal measured in a field $H_{ac} = 1$ Oe at a frequency of 10 Hz. The antiferromagnetic transition temperatures T_N are marked as shown.

small anisotropies which typically showed $\chi_b > \chi_a > \chi_c$. However, occasionally variations of $\pm 5\%$ in the absolute value of $\chi_i(T)$ were observed between different runs for the same crystal axis i that we attribute to sample size and positioning effects (radial off-centering) in the second order gradiometer coils of the Quantum Design MPMS SQUID magnetometer.^{26,27}

The ordering temperatures observed are marked by vertical arrows in Fig. 10 and are highlighted in the plots of $d(\chi T)/dT$ versus T shown in the insets. The various transition temperatures are summarized in Table IV. As is typical for a low-dimensional antiferromagnetic system, the polycrystalline sample shows only a very weak cusp at $T_N = 76$ K due to averaging over the three principal

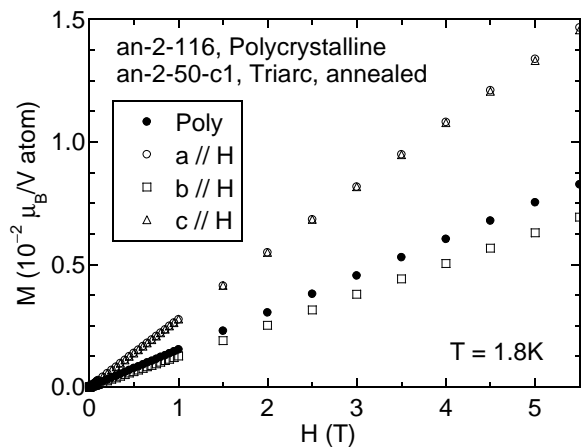


FIG. 12: Magnetization M versus applied magnetic field H isotherms at a temperature of 1.8 K of a polycrystalline sample and of an annealed triarc grown single crystal of CaV_2O_4 .

axis directions, but it is still well-defined as observed in the $d(\chi T)/dT$ vs T plot shown in the inset of Fig. 10(a). In a related study, ^{17}O NMR measurements on a polycrystalline sample of ^{17}O -enriched CaV_2O_4 gave a clear signature of antiferromagnetic ordering at 78 K.¹⁴ In contrast to the polycrystalline sample, the as-grown crystal in Fig. 10(b) shows a clear and distinct antiferromagnetic ordering temperature but with a much lower value $T_N \approx 51$ K. After annealing the crystals, Figs. 10(c) and 10(d) show that T_N increases to ≈ 69 K, closer to that observed in the polycrystalline sample. However, the powder average of the annealed single crystal susceptibility below T_N does not match the susceptibility of the polycrystalline sample. The reason for this disagreement is unclear at this time. In any case the slow upturn in the susceptibility of the powder sample below 40 K in Fig. 10 is evidently intrinsic, due to the powder average of the anisotropic susceptibilities, and is not due to magnetic impurities.

The zero-field-cooled (zfc) and field-cooled (fc) $\chi(T)$ measured in a field of 100 Oe for polycrystalline and single crystal samples of CaV_2O_4 are plotted in Figs. 11(a)–(d). Also shown in Fig. 11(c) is the real part of the ac susceptibility $\chi'_{ac}(T)$ along the easy b -axis direction of the annealed triarc crystal measured in an ac field of amplitude 1 Oe at a frequency of 10 Hz. A small irreversibility is observed in Fig. 11 in all samples between the zfc and fc susceptibilities below ~ 30 K. However, the $\chi'_{ac}(T)$ measurement in Fig. 11(c) does not show any peak in that temperature region, ruling out spin glass-like spin freezing which was suggested to occur in powder samples from earlier reports.^{10,11} The slight irreversibility observed may be associated with antiferromagnetic domain wall effects.

In Fig. 12 we show isothermal $M(H)$ measurements up to $H = 5.5$ T measured at 1.8 K for the polycrystalline sample and for the annealed triarc-grown single crystal. The behavior is representative of all samples measured.

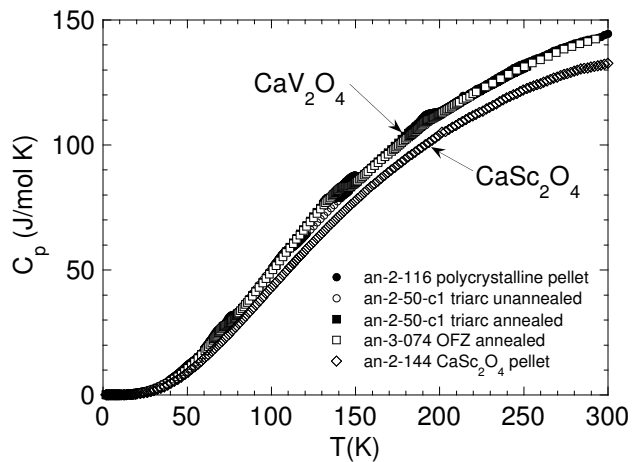


FIG. 13: Heat Capacity C_p versus temperature T in zero magnetic field of one polycrystalline sample and three single crystal samples of CaV_2O_4 and of a polycrystalline sample of isostructural nonmagnetic CaSc_2O_4 . On this scale, the data for the four CaV_2O_4 samples are hardly distinguishable.

We find that M is proportional to H at fields up to at least ~ 2 T, indicating the absence of any significant ferromagnetic impurities and the absence of a ferromagnetic component to the ordered magnetic structure.

B. Heat Capacity Measurements

The heat capacity C_p versus temperature T of a sintered polycrystalline pellet of CaV_2O_4 as well as of crystals (as-grown and annealed) was measured using a Quantum Design PPMS system at $T = 1.8$ to 200–300 K in zero applied magnetic field. The $C_p(T)$ was also measured of a polycrystalline sintered pellet of isostructural (at room temperature) nonmagnetic CaSc_2O_4 whose lattice parameters and formula weight are very similar to those of CaV_2O_4 .²⁸ The CaSc_2O_4 sample was synthesized from Sc_2O_3 (99.99%, Alfa) and CaCO_3 (99.995%, Aithaca) by reacting a stoichiometric mixture in air at 1000 °C for 24 hr and then at 1200 °C for 96 hr with intermediate grindings, and checked for phase purity using powder XRD.

In Fig. 13 we plot the measured $C_p(T)$ of four CaV_2O_4 samples and of isostructural nonmagnetic CaSc_2O_4 . The difference ΔC_p versus T for the four CaV_2O_4 samples is plotted in Fig. 14(a). Here ΔC_p is the difference between the heat capacity of CaV_2O_4 and that of CaSc_2O_4 , but where the temperature axis of C_p for CaSc_2O_4 was multiplied by a scaling factor to take account of the difference in the formula weights of CaV_2O_4 and CaSc_2O_4 . This factor is given by $[M_M(\text{CaSc}_2\text{O}_4)/M_M(\text{CaV}_2\text{O}_4)]^{1/2} = 0.9705$ where M_M is the molar mass of the respective compound. If the lattice heat capacity of CaV_2O_4 and the (renormalized) heat capacity of CaSc_2O_4 had been the same, the difference $\Delta C_p(T)$ would presumably have been the magnetic heat

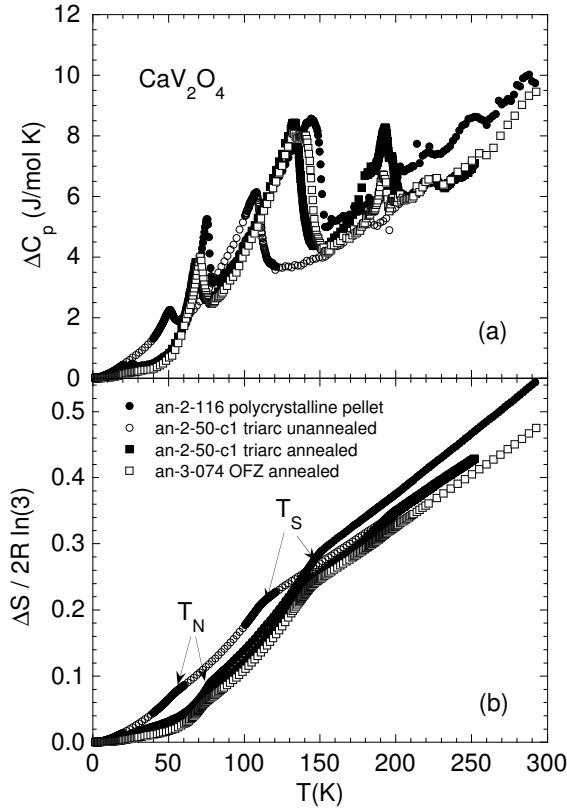


FIG. 14: (a) ΔC_p versus temperature T for four CaV_2O_4 samples. Here ΔC_p is the difference between the heat capacity of CaV_2O_4 and that of CaSc_2O_4 , but where the temperature axis of C_p for CaSc_2O_4 was multiplied by 0.9705 to take account of the difference in the formula weights of CaV_2O_4 and CaSc_2O_4 . (b) Entropy $\Delta S(T)$ associated with the $\Delta C_p(T)$ data in (a), obtained by integrating $\Delta C_p/T$ in (a) versus T . The ΔS is normalized by the entropy $2R \ln(3)$ of two moles of disordered spins $S = 1$, where R is the molar gas constant.

capacity of CaV_2O_4 . However, due to the structural transition at T_S and the transition at T_{S1} , $\Delta C_p(T)$ contains a lattice contribution as well. The lattice contribution to ΔC_p is expected to be minimal at low temperatures, where only the long wavelength acoustic phonon modes are excited, and possibly also above T_{S1} where the two compounds are known to be isostructural.

Figure 14(a) shows that the $\Delta C_p(T)$ data for the four CaV_2O_4 samples are similar except for the different sizes and temperatures of the anomalies associated with three transitions. In order to more clearly illustrate the differences between samples, Fig. 15 shows the same data for each sample but vertically displaced from each other to avoid overlap. The magnetic ordering transition at T_N as well as the ordering temperatures T_S and T_{S1} are clearly evident from the $\Delta C_p(T)$ data in Fig. 15. The ordering temperatures observed are summarized above in Table IV.

The entropy versus temperature associated with the $\Delta C_p(T)$ data of each sample in Fig. 14(a) is shown in

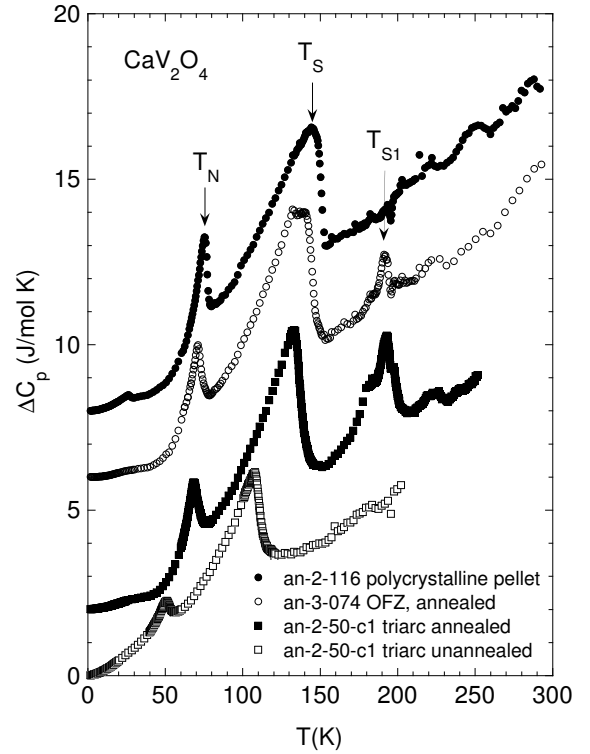


FIG. 15: ΔC_p versus temperature T for four CaV_2O_4 samples. The data are the same as in Fig. 14(a) except for vertical offsets to separate the data sets. The symbol T_N labels the long-range antiferromagnetic transition and T_S labels the high temperature orthorhombic to low temperature monoclinic structural transition. An additional transition at $T_{S1} \sim 200$ K is seen in the two annealed single crystals. The small anomaly for the AFZ crystal and for the triarc crystal that rides on top of the broader peak appear to be intrinsic to CaV_2O_4 . The broad peak in the latter crystal appears to be due to coherently grown V_2O_3 impurity phase that grows during annealing (see text).

Fig. 14(b), obtained from $\Delta S(T) = \int_0^T [\Delta C_p(T)/T] dT$. In Fig. 14(b), ΔS is normalized by the entropy $2R \ln(2S + 1) = 2R \ln(3)$ for two moles of fully disordered spins $S = 1$, where R is the molar gas constant. As noted above, at least at low temperatures, we associate $\Delta S(T)$ with the magnetic entropy of the system. At the antiferromagnetic ordering temperature T_N , the normalized value of $\Delta S(T_N)/2R \ln(3) \approx 6-8\%$ is very small and is about the same for all samples. This small value indicates that short-range antiferromagnetic ordering is very strong above T_N and the data in Fig. 14(b) indicate that the maximum spin entropy of the system is not attained even at room temperature. This is qualitatively consistent with our estimate $J_1 \approx 230$ K obtained below in Sec. IV by comparison of our $\chi(T)$ data with calculations of $\chi(T)$.

The small observed magnetic entropy at T_N is consistent with the values of the heat capacity discontinuities ΔC_{AF} at T_N in Fig. 15, as follows. In mean field theory,

TABLE V: Relative length changes along the orthorhombic a -, b - and c -axis directions and of the volume V that are associated with the three transitions at $T_N \approx 70$ K, $T_S \approx 140$ K, and $T_{S1} \approx 195$ K in annealed triarc CaV_2O_4 single crystal an-2-50-c1. The temperature T range over which the changes were measured are as indicated.

T range (K)	T_N	T_S	T_{S1}
$\Delta a/a$ (10^{-5})	1.2	4.9	-7.5
$\Delta b/b$ (10^{-5})	-4.3	-0.9	-0.1
$\Delta c/c$ (10^{-5})	1.1	19.6	-6.3
$\Delta V/V$ (10^{-5})	-2.0	23.6	-13.9

for a system containing N spins S the discontinuity in the magnetic heat capacity at the ordering temperature for either ferromagnetic or antiferromagnetic ordering is predicted to be²⁹

$$\Delta C_{AF} = \frac{5}{2} N k_B \frac{(2S+1)^2 - 1}{(2S+1)^2 + 1}, \quad (2)$$

where N is the number of spins and k_B is Boltzmann's constant. Using $S = 1$ relevant to V^{+3} and $Nk_B = 2R$, where R is the molar gas constant, one obtains $\Delta C_{AF} = 4R = 33.3$ J/mol K, where a "mol" refers to a mole of CaV_2O_4 formula units. From Fig. 15, the experimental ΔC_{AF} is about 0.5 to 2 J/mol K, which is only 1.5–6% of the mean field value. This small jump in $C_p(T_N)$ is consistent with the above small value of $S(T_N)$. When short range magnetic ordering removes most of the magnetic entropy of a system at high temperatures, then thermal effects associated with three-dimensional magnetic ordering of the system at low temperatures will necessarily be much smaller than otherwise expected.

C. Thermal Expansion Measurements

The thermal expansion of the annealed triarc grown CaV_2O_4 crystal an-2-50-c1 was measured versus temperature using capacitance dilatometry³⁰ from 1.8 to 300 K along the three orthorhombic axes a , b and c . The crystal is the same annealed triarc crystal measured by magnetic susceptibility and heat capacity in Figs. 10 and 11(c) and in Figs. 13–15, respectively. In Fig. 16 the linear coefficients of thermal expansion are plotted versus temperature (left-hand scale), along with the volume thermal expansion coefficient (right-hand scale). At high temperatures $T \sim 300$ K the α values tend to become temperature independent. Below 200 K, the ordering transitions observed above in the magnetic susceptibility and heat capacity are reflected in distinct anomalies in the thermal expansion coefficients at the corresponding temperatures. The ordering temperatures observed are summarized above in Table IV.

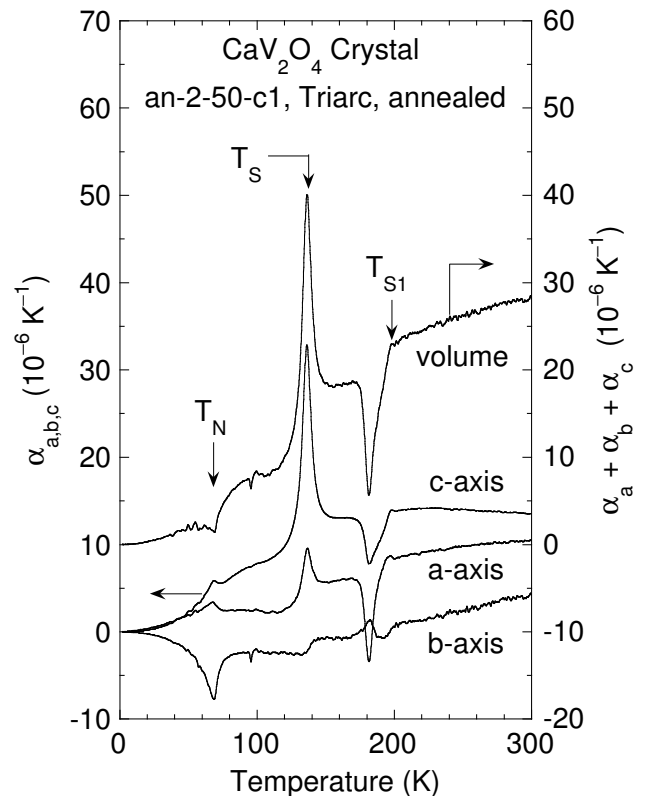


FIG. 16: Coefficients of linear thermal expansion $\alpha_{a,b,c}$ of an annealed single crystal of CaV_2O_4 measured along the orthorhombic a , b , and c -axes versus temperature (left-hand scale), and the volume expansion coefficient $\alpha_a + \alpha_b + \alpha_c$ versus temperature (right-hand scale).

The normalized length changes along the orthorhombic a , b and c axis directions and the normalized change in the volume V associated with the three transitions at T_N , T_S and T_{S1} are listed in Table V. These changes were calculated by determining the areas under the respective peaks in the thermal expansion coefficients in Fig. 16, and then subtracting the estimated respective background changes over the same temperature intervals.

IV. ANALYSIS OF EXPERIMENTAL DATA

A. Origin of the Transition at $T_{S1} \sim 200$ K in Annealed CaV_2O_4 Single Crystals

From Table V above, the relative volume change of the annealed triarc crystal an-2-50-c1 on heating through T_{S1} from the thermal expansion data is $\Delta V/V \approx -1.4 \times 10^{-4}$. This value is about 1% of the value for pure V_2O_3 at its transition.²¹ The height of the heat capacity anomaly above "background" in Fig. 15 for this crystal is ≈ 2.5 J/mol K, which is about 0.8% of the value²³ at the structural transition for pure V_2O_3 . These estimates are both consistent with our estimates from x-ray diffraction

data in Sec. II of a 1–2 percent volume fraction of V_2O_3 in this crystal. Our data therefore indicate that for the annealed triarc-grown crystal (an-2-50-c1), the anomalous features found above in the heat capacity and thermal expansion data at T_{S1} arise mainly from this transition in the V_2O_3 impurity phase.

Furthermore, the temperature dependences of the linear thermal expansion coefficients at the transition $T_{S1} \approx 200$ K in Fig. 16 are significantly different than near the transitions $T_N \approx 70$ K and $T_S \approx 140$ K. There appears to be a discontinuity in the slopes of $\alpha_i(T)$ as the transition T_{S1} is approached from above, whereas a continuous change in the slopes occurs as T_S and T_N are approached from above. The reason for this difference is evidently that the former transition is mainly due to the *first order* structural transition in the V_2O_3 coherently-grown impurity phase in this annealed crystal as investigated previously in Sec. IIC 1, whereas the latter two transitions are *second order*.

However, we also found in Sec. II that for the annealed floating-zone crystal (an-3-074 OFZ), the structural transition of the V_2O_3 impurity phase was reduced by ~ 60 K from that of the V_2O_3 impurity phase in the annealed triarc grown crystal, and hence cannot be responsible for heat capacity anomaly at $T_{S1} \sim 200$ K for the annealed float-zone crystal in Fig. 15. Indeed, the relatively small heat capacity anomaly at T_{S1} in Fig. 15 for the float-zone crystal appears to also be present at the same temperature for the annealed triarc-grown crystal, but rides on top of a broader anomaly that is evidently due to the structural transition of the V_2O_3 impurity phase in that crystal. Furthermore, the double peak structure in the heat capacity for the annealed triarc crystal at $T_S \approx 140$ K evidently arises due to the overlap of the onsets of the structural transitions in V_2O_3 and CaV_2O_4 .

An issue of interest is the cause(s) of the variability in the structural rhombohedral-to-monoclinic transition temperature of the coherently grown V_2O_3 impurity phase in our annealed CaV_2O_4 crystals. Due to the first order nature of the transition, the transition is hysteretic. The transition temperature of bulk stoichiometric V_2O_3 has been reported to be at ≈ 170 K on heating and ≈ 150 K on cooling.^{23,31,32,33} The transition temperature *decreases* rapidly under pressure.³⁴ A pressure of only 9 kbar lowers the transition temperature by 60 K, and the transition is completely suppressed at a pressure of ≈ 20 kbar.³⁴ The transition temperature is also rapidly *suppressed* if the sample contains V vacancies; a crystal of composition $V_{1.985}O_3$ showed a transition temperature of ≈ 50 K.³³ Furthermore, it was found that when V_2O_3 is epitaxially grown on $LiTaO_3$, the transition temperature is *enhanced* from the bulk value by 20 K.²⁵ Given the possibilities of compressive or tensile forces acting on the V_2O_3 due to the epitaxial relationship of the V_2O_3 impurity with the CaV_2O_4 host and the possibility of nonstoichiometry of the V_2O_3 impurity phase, one can see how the transition temperature of the V_2O_3 might be *depressed or enhanced* from the bulk value by ≈ 30 K as

we found for the coherently grown V_2O_3 impurity phases in our two annealed crystals in Sec. IIC.

In summary, then, it appears that there is an intrinsic phase transition in the two annealed CaV_2O_4 crystals at about 200 K that has no obvious source. We speculate that this transition may be the long-sought chiral phase transition originally postulated by Villain,⁹ where there is long-range chiral order but no long-range spin order below the transition temperature, and the long-range chiral order is lost above the transition temperature.

B. Magnetic Susceptibility and Magnetic Heat Capacity

In separate experiments to be described elsewhere,¹⁷ we have carried out inelastic neutron scattering measurements of the magnetic excitation dispersion relations for CaV_2O_4 single crystals. We find that the dispersion along the c -axis (in the vanadium chain direction) is significantly larger than in the two perpendicular directions. Above the Néel temperature T_N , the magnetic susceptibility in Fig. 10 is nearly isotropic. Thus a quasi-one-dimensional Heisenberg model appears to be appropriate for the spin interactions in CaV_2O_4 .

The crystal structure suggests the presence of spin $S = 1$ zigzag spin chains along the orthorhombic c -axis. We report here exact diagonalization (ED) calculations of the magnetic spin susceptibility versus temperature $\chi(T)$ and the magnetic heat capacity $C(T)$ of spin $S = 1$ J_1 - J_2 Heisenberg chains containing $N = 8, 10,$ and 12 spins for J_2/J_1 ratios from -1 to 5 , and containing 14 spins for $J_2/J_1 = 0$. We also report the results of quantum Monte Carlo (QMC) simulations of $\chi(T)$ and $C(T)$. These simulations were carried out with the ALPS directed loop application³⁵ in the stochastic series expansion framework³⁶ for chains with $N = 30$ and 60 spins and $J_2/J_1 = 0$. Here J_1 and J_2 are the nearest-neighbor and next-nearest-neighbor interactions on a linear chain, respectively. The spin Hamiltonian is the $\lambda = 1$ special case of Eq. (1), given by

$$\mathcal{H} = \sum_{i=1}^N (J_1 \mathbf{S}_i \cdot \mathbf{S}_{i+1} + J_2 \mathbf{S}_i \cdot \mathbf{S}_{i+2}), \quad (3)$$

where \mathbf{S} is a spin-1 operator. Periodic boundary conditions are imposed, so the chains become rings. J_1 is always positive (antiferromagnetic) whereas J_2 was taken to be either positive or negative (ferromagnetic). This chain is topologically the same as a zigzag chain in which J_1 is the nearest-neighbor interaction between the two legs of the zigzag chain and J_2 is the nearest-neighbor interaction along either leg of the zigzag chain. For $J_2 = 0$, the N spins are all part of the same nearest-neighbor exchange (J_1) chain. For $J_1 = 0$, two independent isolated equivalent chains are formed, each containing $N/2$ spins and with nearest-neighbor exchange J_2 . This effect can be quantified using the $T = 0$ correlation length ξ which

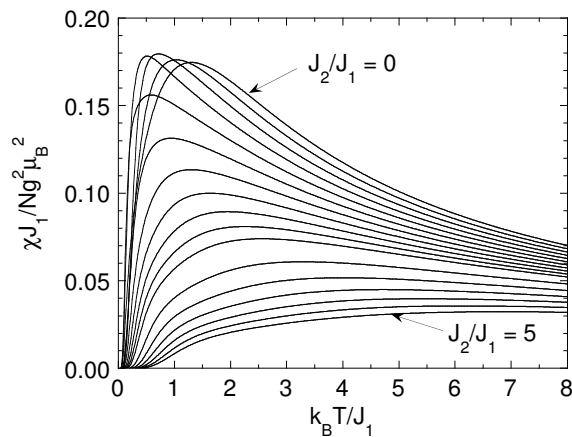


FIG. 17: Calculated magnetic spin susceptibility χ for spin $S = 1$ J_1 - J_2 Heisenberg chains containing $N = 12$ spins versus temperature T , where J_1 and J_2 are the nearest-neighbor and next-nearest-neighbor exchange interactions in the chain. The curves from top to bottom on the right are for $J_2/J_1 = 0, 0.2, 0.4, \dots, 2.0, 2.5, \dots, 5.0$.

has been computed in Ref. 37. We find that we can reach ratios N/ξ which are at least 2 for $J_2/J_1 \lesssim 0.6$ whereas ξ becomes comparable to or even bigger than the system sizes N which are accessible by ED for larger J_2/J_1 . Accordingly, our finite chain data become a poorer approximation to the infinite J_1 - J_2 chain for large J_2/J_1 . This is exemplified below in Fig. 20 where the data for chains containing different numbers N of spins exhibit an increasing divergence from each other with increasing J_2/J_1 .

We will compare the spin susceptibility calculations with the experimental magnetic susceptibility data to estimate the J_1 and J_2/J_1 values in the J_1 - J_2 chain model for CaV_2O_4 . These values will also be used as input to compare the calculated magnetic heat capacity versus temperature with the experimental heat capacity data.

1. Magnetic Susceptibility

The calculated magnetic spin susceptibility $\chi(T)$ data for the spin $S = 1$ J_1 - J_2 Heisenberg chain model are in the dimensionless form

$$\frac{\chi J_1}{N g^2 \mu_B^2} \text{ versus } \frac{k_B T}{J_1}, \quad (4)$$

where N is the number of spins, g is the spectroscopic splitting factor (g -factor) of the magnetic moments for a particular direction of the applied magnetic field with respect to the crystal axes, μ_B is the Bohr magneton, and k_B is Boltzmann's constant. Calculated $\chi(T)$ data sets for $N = 12$ were obtained by exact diagonalization assuming periodic boundary conditions (ring geometry) for J_2/J_1 ratios of $-1, -0.8, \dots, 2.0, 2.5, \dots, 5$. Examples of the calculations for a selection of J_2/J_1 values are

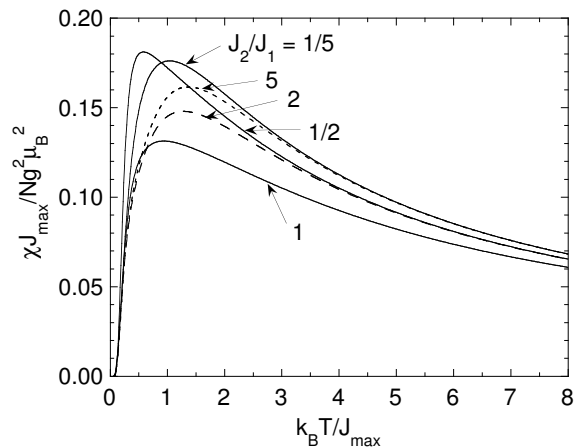


FIG. 18: Magnetic susceptibility χ versus temperature T for the spin $S = 1$ J_1 - J_2 Heisenberg chain containing $N = 12$ spins. Here, $J_{\max} = \max(J_1, J_2)$. Pairs of curves for J_2/J_1 ratios that are reciprocals of each other become the same at high temperatures.

shown in Fig. 17. Each chain has an energy gap (spin gap) from the nonmagnetic singlet ground state to the lowest magnetic excited states.³⁷ No interchain (between adjacent zigzag chains) interactions are included in the calculations. These calculations are not expected to apply to our system at low temperatures where we see long-range antiferromagnetic ordering. However, we expect to be able to obtain approximate estimates of J_1 and J_2 by fitting the observed susceptibility data around the broad peak in the susceptibility at ≈ 300 K.

At high temperatures $k_B T \gg J_{\max}$, where $J_{\max} = \max(J_1, J_2)$, one expects that the calculated χJ_{\max} versus $k_B T / J_{\max}$ should be nearly the same upon interchange of J_1 and J_2 , i.e., the same for pairs of J_2/J_1 ratios that are reciprocals of each other. [This is because all spins in the zigzag chain are equivalent, and at high temperatures the Curie-Weiss law is obtained. The Weiss temperature θ only depends on the numbers of nearest neighbors z to a given spin and the corresponding interaction strengths J ($\theta \sim z_1 J_1 + z_2 J_2$ with $z_1 = z_2 = 2$), which is invariant upon interchange of J_1 and J_2 .] This expectation is confirmed in Fig. 18 where such plots are shown for $J_2/J_1 = 1/5$ and 5; $1/2$ and 2; and 1. The data for $J_2/J_1 = 1/2$ and 2, and for $J_2/J_1 = 1/5$ and 5, are seen to be about the same for temperatures $k_B T / J_{\max} \gtrsim 4$, respectively.

The experimental magnetic susceptibility data of CaV_2O_4 will be fitted below by the calculated susceptibility $\chi(T)$ of a single $S = 1$ chain ($J_2/J_1 = 0$). Such integer-spin chains are known as Haldane chains.³⁸ We will therefore test here the sensitivity of the calculations to the number of spins N in the chain for this fixed J_2/J_1 value. Shown in Fig. 19 are exact diagonalization (ED) calculations of $\chi(T)$ for $J_2/J_1 = 0$ and $N = 12$ and 14, and quantum Monte Carlo (QMC) simulations for $J_2/J_1 = 0$ and $N = 60$. On the scale of the fig-

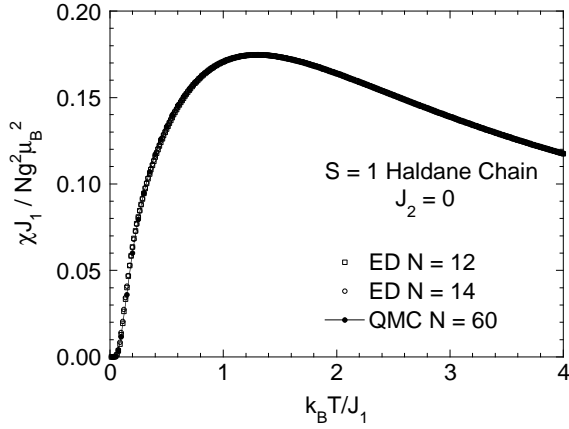


FIG. 19: Magnetic susceptibility χ versus temperature T calculations for the spin $S = 1$ Heisenberg chain with nearest neighbor exchange interaction J_1 and next-nearest-neighbor interaction $J_2 = 0$. The calculations were carried out using exact diagonalization (ED) for $N = 12$ and 14 , and by quantum Monte Carlo (QMC) for $N = 60$.

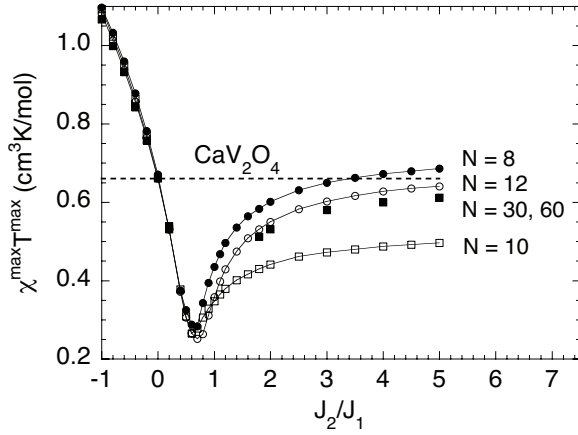


FIG. 20: The product $\chi^{\max} T^{\max}$ versus J_2/J_1 for the spin $S = 1$ J_1 - J_2 Heisenberg chain containing $N = 8, 10, 12, 30$ or 60 spins, where we have assumed $N = 2N_A$ and $g = 1.97$. The data for $N = 8, 10$, and 12 were obtained using exact diagonalization calculations. The data for $N = 30$ and 60 were obtained from quantum Monte Carlo simulations; most of these data were obtained for $N = 60$, except for $J_2/J_1 = 0.2, 1.8$ and 2 where we used $N = 30$. The horizontal dashed line is the experimental value of $\chi^{\max} T^{\max}$ for CaV_2O_4 from Eq. (7). Comparison of this experimental value with the calculations indicates that within the J_1 - J_2 model, $J_2/J_1 \approx 0$ (or $J_1/J_2 \approx 0$) in CaV_2O_4 .

ure, the results of the three calculations can hardly be distinguished. These data are fully consistent with previous transfer-matrix renormalization-group results for $\chi(T)$.^{39,40} In Table VI, the values of the maxima in the magnetic susceptibility χ^{\max} and also of the magnetic heat capacity C^{\max} (see below) and the temperatures T_χ^{\max} and T_C^{\max} at which they respectively occur are listed for the different calculations. For all three cal-

culations, the maximum in the susceptibility occurs at about the same temperature $k_B T_\chi^{\max}/J_1 \approx 1.30$, which may be compared with previous values of 1.35 (Ref. 41) and $1.32(3)$.⁴² Probably the most accurate values for the susceptibility are those of Ref. 40, as listed in Table VI.

From the theoretical $\chi(T)$ data, for each value of J_2/J_1 one can obtain the value of the normalized temperature $k_B T^{\max}/J_1$ at which the maximum in the susceptibility occurs, and the normalized value of the susceptibility $\chi^{\max} J_1 / N g^2 \mu_B^2$ at the maximum. For a given value of J_2/J_1 , the product of these two values is a particular dimensionless number

$$\frac{\chi^{\max} T^{\max}}{N g^2 \mu_B^2 / k_B} \quad (5)$$

that does not contain either exchange constant.

The spectroscopic splitting tensor (g -tensor) for vanadium cations is found to not depend much on either the oxidation (spin) state of the V cation or on its detailed environment in insulating hosts. The physical origin of this insensitivity is the small magnitude of the spin-orbit coupling constant for the vanadium atom. Typical values for the spherically-averaged g -factor $\langle g \rangle$ are between approximately 1.93 and 1.97 , with the individual components of the diagonal g -tensor lying between 1.90 and 2.00 . For example, for V^{+2} in single crystals of AgCl , one obtains $\langle g \rangle = 1.970(3)$;⁴³ for V^{+3} in guanidinium vanadium sulfate hexahydrate, $\langle g \rangle = 1.94(1)$;⁴⁴ for V^{+4} in TiO_2 , $\langle g \rangle = 1.973(4)$.⁴⁵

On the basis of the above discussion we set $g = 1.97$ for the V^{+3} spin $S = 1$ in Eq. (5). Then setting $N = 2N_A$, where N_A is Avogadro's number and the factor of 2 comes from two atoms of V per formula unit of CaV_2O_4 , the expression in Eq. (5) becomes

$$\frac{\chi^{\max} T^{\max}}{2.91 \text{ cm}^3 \text{ K/mol}}, \quad (6)$$

where a “mol” refers to a mole of CaV_2O_4 formula units. Then from Eq. (6) and the calculated $\chi(T)$ data for different values of J_2/J_1 , the calculated $\chi^{\max} T^{\max}$ versus J_2/J_1 for CaV_2O_4 is shown in Fig. 20. From the figure, the dependence of $\chi^{\max} T^{\max}$ on J_2/J_1 is about the same for $N = 8, 10$, and 12 for $J_2/J_1 \lesssim 0.6$ which is consistent with a short correlation length $\xi \lesssim 6$ for $0 \leq J_2/J_1 \leq 0.6$ (see Ref. 37). However, the curves for the different values of N are quite different at larger values of J_2/J_1 ; the behavior versus N even becomes nonmonotonic in this parameter region. The QMC results also shown in Fig. 20 nevertheless indicate that the ED calculations for $N = 12$ sites yield a good approximation to the infinite N limit also for $J_2/J_1 \geq 1.8$. Unfortunately, the QMC sign problems are so severe in the region $0.2 < J_2/J_1 < 1.8$ that here we cannot resolve the maximum of χ with our QMC simulations.

The experimental susceptibility $\chi_{\text{exp}}(T)$ data for CaV_2O_4 in Fig. 10 can be written as the sum $\chi_{\text{exp}}(T) = \chi(T) + \chi_0$, where $\chi(T)$ is the spin susceptibility (which is

TABLE VI: Calculated values of the maxima in the magnetic spin susceptibility χ^{\max} and magnetic heat capacity C^{\max} and temperatures T_X^{\max} and T_C^{\max} at which they occur, respectively, for the linear spin $S = 1$ Heisenberg chain (Haldane chain) with nearest-neighbor exchange interaction J_1 and next-nearest-neighbor interaction $J_2 = 0$. The results of exact diagonalization (ED) and quantum Monte Carlo (QMC) calculations are shown. Here N is the number of spins in the chain, g is the g -factor, μ_B is the Bohr magneton, and k_B is Boltzmann's constant. Also included are the results of Ref. 40, which are probably the most accurate values currently available for the susceptibility.

	$\frac{\chi^{\max} J_1}{N g^2 \mu_B^2}$	$\frac{k_B T_X^{\max}}{J_1}$	$\frac{C^{\max}}{N k_B}$	$\frac{k_B T_C^{\max}}{J_1}$
QMC $N = 60$	0.174686(9)	1.301(10)	0.5431(4)	0.857(10)
ED $N = 12$	0.174662	1.2992	0.5520	0.8295
ED $N = 14$	0.174677	1.2980	0.5466	0.8398
Ref. 40	0.17496(2)	1.2952(16)		

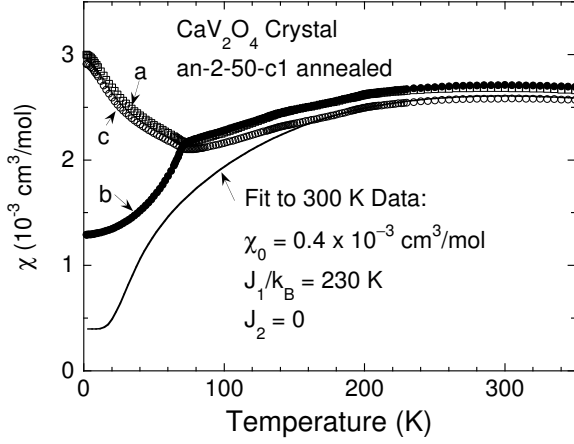


FIG. 21: Calculated magnetic susceptibility χ versus temperature T for the J_1 - J_2 chain with $J_1/k_B = 230$ K, $J_2 = 0$, and $g = 1.97$, and with a temperature-independent orbital contribution $\chi_0 = 0.4 \times 10^{-3} \text{ cm}^3/\text{mol}$ (solid curve). The calculated spin susceptibility at $T = 0$ is zero, so the zero-temperature value of the calculated solid curve is χ_0 . Experimental data for annealed CaV_2O_4 crystal 2-50-c1 from Fig. 10 are also shown. Comparison of these data for $T \rightarrow 0$ with the calculated curve shows that the spin susceptibility along the easy b -axis of CaV_2O_4 is rather large for $T \rightarrow 0$.

the part calculated above) and χ_0 is the temperature-independent orbital susceptibility. From the data in Ref. 46 for V_2O_3 , we estimate $\chi_0 \sim 0.4 \times 10^{-3} \text{ cm}^3/\text{mol}$ for CaV_2O_4 . From Fig. 10 we then obtain the experimental value for the *spin* susceptibility at the maximum $\chi^{\max} \approx 2.2 \times 10^{-3} \text{ cm}^3/\text{mol}$ and for the temperature at the maximum $T_X^{\max} \approx 300$ K, yielding for CaV_2O_4

$$\chi^{\max} T^{\max} \approx 0.66 \text{ cm}^3 \text{ K/mol} . \quad (7)$$

Comparison of this value with the theoretical spin susceptibility data in Fig. 20 yields $J_2/J_1 \approx 0$ (or $J_1/J_2 \approx 0$). This ratio of J_2/J_1 is quite different from the value of

unity that we and others^{10,11} initially expected. The temperature $T_X^{\max} \approx 300$ K, combined with $k_B T_X^{\max}/J_1 \approx 1.30$ from Table VI, yields $J_1/k_B = 230$ K. Although the numerical results shown in Fig. 20 are the least accurate in the vicinity of $J_2/J_1 \approx 1$, it seems rather unlikely that the value of $\chi^{\max} T^{\max}$ obtained from the J_1 - J_2 chain model in the region $0.6 \lesssim J_2/J_1 \lesssim 1.8$ could be consistent with the value in Eq. (7) expected for CaV_2O_4 .

The calculated total susceptibility versus temperature for $J_1/k_B = 230$ K, $J_2 = 0$ and $\chi_0 = 0.4 \times 10^{-3} \text{ cm}^3/\text{mol}$ is shown in Fig. 21. Also shown are the experimental susceptibility data for annealed CaV_2O_4 crystal an-2-50-c1 from Fig. 10, where an excellent fit of the average anisotropic $\chi(T)$ data near 300 K is seen.

Above the Néel temperature, one sees from Figs. 10 and 21 that the susceptibility is nearly isotropic. The relatively small anisotropy observed can come from anisotropy in the orbital Van Vleck paramagnetic susceptibility, from g -anisotropy arising from spin-orbit interactions, from single-ion anisotropy of the form $DS_z^2 + E(S_x^2 - S_y^2)$, and/or from anisotropy in the spin exchange part of the spin Hamiltonian. The relative importances of these sources to the observed susceptibility anisotropies are not yet clear. The experimental data below 200 K in Fig. 21 increasingly deviate from the fit with decreasing temperature. This suggests that other interactions besides J_1 and J_2 and/or the presence of magnetic anisotropies may be important to determining the spin susceptibility above T_N in CaV_2O_4 .

For collinear antiferromagnetic (AF) ordering, one nominally expects the spin susceptibility along the easy axis to go to zero as $T \rightarrow 0$. Comparison of the theoretical curve with the experimental easy axis (b -axis) data $\chi_b(T)$ in Fig. 21 indicates that the zero-temperature b -axis spin susceptibility is not zero, but is instead a rather large value $\chi_b^{\text{spin}}(T \rightarrow 0) \approx 0.9 \times 10^{-3} \text{ cm}^3/\text{mol}$. This finite spin susceptibility indicates either that the spin structure in the AF state is not collinear, that not all vanadium spins become part of the ordered magnetic structure below T_N , and/or that quantum fluctuations are present that induce a nonzero spin susceptibility. Such quantum fluctuations can arise from the low-dimensionality of the spin lattice and/or from frustration effects. As discussed in the Introduction, our recent NMR and magnetic neutron diffraction experiments on single crystal CaV_2O_4 indicated that the magnetic structure at 4 K is noncollinear,^{14,15} which can at least partially explain the nonzero spin susceptibility along the (average) easy b -axis at low temperatures. In addition, the reduction in the local ordered moment 1.0–1.6 $\mu_B/(\text{V atom})$ of the *ordered* vanadium spins found in these studies from the expected value $gS\mu_B = 2 \mu_B/(\text{V atom})$ suggests that quantum zero-point spin fluctuations could be strong and could contribute to the large finite $\chi_b^{\text{spin}}(T \rightarrow 0)$.

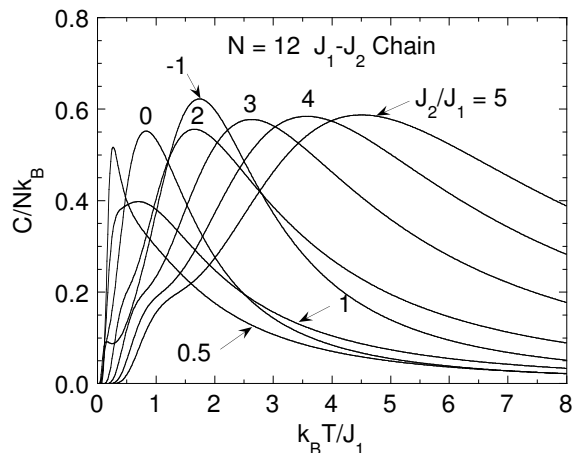


FIG. 22: Magnetic heat capacity C versus temperature T for the spin $S = 1$ J_1 - J_2 Heisenberg chain with J_2/J_1 values from -1 to 5 , calculated using exact diagonalization with $N = 12$. Here N is the number of spins, k_B is Boltzmann's constant, and $J_1 > 0$ and J_2 are the nearest-neighbor and next-nearest-neighbor exchange interactions, respectively.

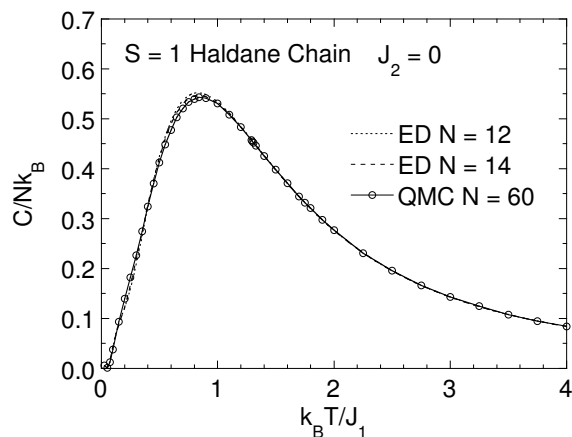


FIG. 23: Magnetic heat capacity C versus temperature T for the $S = 1$ J_1 - J_2 chain with $J_2/J_1 = 0$ (“Haldane chain”), calculated using exact diagonalization (ED) with $N = 10$ and 12 , and quantum Monte Carlo (QMC) simulations for $N = 60$.

2. Magnetic Heat Capacity

The magnetic heat capacity C versus temperature T was calculated by exact diagonalization for $N = 12$ spins $S = 1$ over the range $-1 \leq J_2/J_1 \leq 5$. Representative results are plotted in Fig. 22. The variation in $C(T)$ with N is illustrated in Fig. 23 for $J_2/J_1 = 0$ and $N = 12$ and 14 from exact diagonalization calculations, and for $N = 60$ from quantum Monte Carlo simulations. The data for the different N are seen to be nearly the same. The values of the maxima C^{\max} in the magnetic heat capacity and the temperatures T_C^{\max} at which they occur are listed above in Table VI. Our results for the specific heat are consistent with previous transfer-

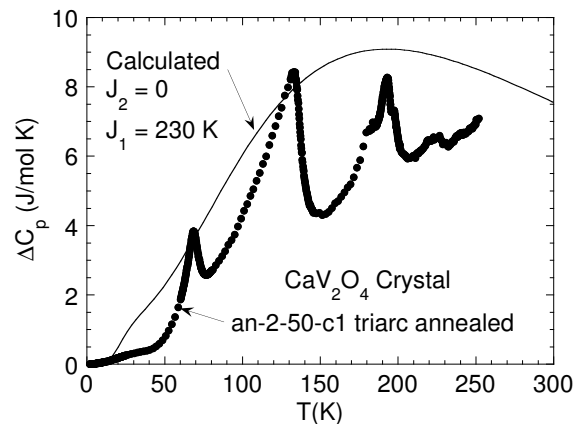


FIG. 24: Magnetic heat capacity C versus temperature T for the spin $S = 1$ J_1 - J_2 chain with $J_2/J_1 = 0$ and $J_1/k_B = 230$ K, calculated using exact diagonalization with $N = 14$ (solid curve) from Fig. 23. The data points are the $\Delta C(T)$ data for annealed crystal an-2-50-c1 from Fig. 15.

matrix renormalization-group computations.^{39,40} The two transfer-matrix renormalization-group results differ at *high* temperatures. Our QMC results for C obtained from rings with $N = 60$ sites are in better agreement with the older results which apply to the infinite N limit³⁹ than the more recent results obtained for open chains with $N = 64$ sites.⁴⁰ The $C(T)$ data in Ref. 40 were calculated from a numerical derivative which resulted in systematic errors in the data at high temperatures.⁴⁷

We cannot confidently derive the exchange constants in CaV_2O_4 from fits of our heat capacity data by the theory. Extraction of the magnetic part of the experimental heat capacity is tenuous because of the presence of the orthorhombic to monoclinic structural transition at $T_S \approx 150$ K and the transition(s) at $T_{S1} \approx 200$ K. Therefore the relationship of the heat capacities $\Delta C(T)$ in Figs. 14(a) and 15 to the magnetic heat capacities of the samples is unclear. Here, we will just compare the theoretical magnetic heat capacity calculated for the exchange constants $J_1 = 230$ K and $J_2 = 0$, that were already deduced in the previous section, with the experimental $\Delta C(T)$ data to see if theory and experiment are at least roughly in agreement. This comparison is shown in Fig. 24 for annealed CaV_2O_4 crystal an-2-50-c1 from Fig. 15. Overall, the theory and experimental data have roughly the same magnitude, but the data are systematically below the theoretical prediction. This is likely caused by the heat capacity of the nonmagnetic reference compound CaSc_2O_4 being somewhat different from the lattice heat capacity of CaV_2O_4 . We note from Fig. 13 that a difference of 5 J/mol K between the theory and experiment in Fig. 24 is only about 5% of the total heat capacity of the samples at 200 K. In addition, we have not included in the theory interchain couplings that lead to long-range antiferromagnetic order, or the effect of the magnetic ordering on the heat capacity including the effect of the energy gap in the spin wave spectrum below

T_N .

C. Interchain Coupling

Within the $S = 1$ J_1 - J_2 Heisenberg spin chain model, we found above that $J_2/J_1 \approx 0$ and $J_1 \approx 230$ K in CaV_2O_4 near room temperature. Thus the crystallographic zigzag vanadium chains in CaV_2O_4 act like $S = 1$ linear spin chains with nearest-neighbor interaction J_1 . This is a so-called Haldane chain³⁸ with a nonmagnetic singlet ground state and an energy gap for spin excitations given by^{48,49} $\approx 0.4105J_1$. An interchain coupling J_\perp must be present in order to overcome this spin gap and induce long-range antiferromagnetic ordering at T_N . Pedrini *et al.*^{42,50} have recently estimated the dependence of T_N/J_1 on J_\perp/J_1 using a random-phase approximation for the interchain coupling for $S = 1$ Haldane chains. Using our values $T_N = 68$ K, $J_1 = 230$ K and $T^{\text{max}} = 300$ K, we obtain $J_\perp/J_1 \approx 0.04$ and $J_\perp = 5$ – 10 K. However, it should be emphasized that the treatment of Refs. 42 and 50 assumes a nonfrustrated interchain coupling geometry such that the result $J_\perp \approx 10$ K should be considered as a lower bound. Still, the value of J_\perp/J_1 is sufficiently small that a redetermination of J_2/J_1 and J_1 , from a J_1 - J_2 - J_\perp model fitted to the observed susceptibility data for CaV_2O_4 near room temperature, would yield very similar values of J_2/J_1 and J_1 to those we have already estimated using the isolated chain J_1 - J_2 model. Additional and more conclusive information about the interchain coupling strength(s) will become available from analysis of inelastic neutron scattering measurements of the magnetic excitation dispersion relations.¹⁷

V. SUMMARY

We have synthesized the $S = 1$ spin chain compound CaV_2O_4 in high purity polycrystalline form and as single crystals. Our magnetic susceptibility $\chi(T)$ and ac magnetic susceptibility $\chi_{\text{ac}}(T)$ measurements do not show any signature of a spin glass-like transition around 20 K that was previously reported.^{10,11} We instead observe long-range antiferromagnetic ordering at sample-dependent Néel temperatures $T_N \approx 50$ – 70 K as shown in Table IV. The Néel temperature and the orthorhombic-to-monoclinic structural transition temperature T_S in Table IV both show a large systematic variation between different samples. Those temperatures for an unannealed crystal are each less than those for an annealed crystal which in turn are less than those for a sintered polycrystalline sample. The cause of these large temperature differences, especially between as-grown and annealed single crystals, is unclear. The transition temperature differences may arise from small changes in oxygen stoichiometry ($\lesssim 1$ at.%, below the threshold of detection by TGA or XRD) and/or from structural strain, both of which may be reduced upon annealing the as-grown crystals at

1200 °C in 5% H_2/He . In addition, other small chemical differences and/or structural defects may be relevant.

Our heat capacity $C_p(T)$, linear thermal expansion $\alpha(T)$, and $\chi(T)$ measurements reveal distinct features at the orthorhombic-to-monoclinic structural transition temperature T_S identified from our diffraction studies.¹⁶ We inferred from a combination of structural studies and physical property measurements that the origin of the third transition at $T_{S1} \approx 200$ K in one of our annealed crystals was mostly due to the structural transition in the V_2O_3 impurity phase that grew coherently upon annealing the crystal. In the other annealed crystal, we ruled out this source and we are thus left with a transition at T_{S1} with unknown origin. We speculate that this transition may be the long-sought chiral phase transition originally postulated by Villain in 1977.⁹

The $\chi(T)$ shows a broad maximum at about 300 K indicating short-range antiferromagnetic (AF) ordering in a low-dimensional antiferromagnet as previously observed^{10,11} and the $\chi(T)$ above T_N in single crystals is nearly isotropic. The anisotropic $\chi(T)$ below T_N shows that the (average) easy axis of the antiferromagnetic structure is the orthorhombic b -axis. The magnetic spin susceptibility along this axis is found to be a large finite value for $T \rightarrow 0$, instead of being zero as expected for a classical collinear antiferromagnet. This result is consistent with our observed noncollinear magnetic structure below T_N .^{14,15} In view of the fact that CaV_2O_4 is a low-dimensional spin system, quantum fluctuations could also contribute to both the observed reduced zero temperature ordered moment and the relatively large zero temperature spin susceptibility.

We analyzed the $\chi(T)$ data near room temperature in terms of theory for the $S = 1$ J_1 - J_2 linear Heisenberg chain, where J_1 (J_2) is the (next-)nearest-neighbor interaction along the chain. We obtain $J_1/k_B \approx 230$ K, but surprisingly $J_2/J_1 \approx 0$ (or $J_1/J_2 \approx 0$), so the exchange connectivity of the spin lattice appears to correspond to linear $S = 1$ Haldane chains instead of zigzag spin chains as expected from the crystal structure. This result is consistent with analysis of our high temperature (up to 1000 K) magnetic susceptibility measurements on single crystal CaV_2O_4 .¹⁵ We estimated here the coupling J_\perp between these chains that leads to long-range AF order at T_N to be $J_\perp/J_1 \gtrsim 0.04$, i.e., only slightly larger than the value $J_\perp/J_1 \approx 0.02$ needed^{42,50} to eliminate the energy gap (Haldane gap) for magnetic excitations.

From our $C_p(T)$ measurements, the estimated molar magnetic entropy at T_N is only $\approx 8\%$ of its maximum value $2R\ln(2S + 1) = 2R\ln(3)$, where R is the molar gas constant, and the heat capacity jump at T_N is only a few percent of the value expected in mean field theory for $S = 1$. Both results indicate strong short range antiferromagnetic order above T_N and large values J_1 and/or $J_2 > 100$ K, consistent with the $\chi(T)$ data. We also compared the $C_p(T)$ data with the theoretical prediction for the magnetic heat capacity using the exchange constants found from the magnetic susceptibility analysis,

and rough agreement was found. However, this comparison is not very precise or useful because the structural transition at $T_S \sim 150$ K and the transition(s) at $T_{S1} \sim 200$ K for our two annealed single crystals, make large contributions to $C_p(T)$. In addition, the accuracy of the measured heat capacity of the nonmagnetic reference compound CaSc_2O_4 in representing the lattice heat capacity of CaV_2O_4 is unknown. Thus extracting the magnetic part of the heat capacity at high temperatures from the observed $C_p(T)$ data for comparison with theory is ambiguous.

In closing, we note the following additional issues that could usefully be addressed in future work. Our analyses of our $\chi(T)$ data for CaV_2O_4 to obtain the exchange constants J_1 and J_2 were based on fitting the experimental $\chi(T)$ data only near room temperature, since our calculations of $\chi(T)$ all showed nonmagnetic singlet ground states, contrary to observation, and could not reproduce the observed antiferromagnetic ordering at low temperatures. Calculations containing additional interactions (see also below) and/or anisotropies are needed for comparison with the lower temperature data.

The orthorhombic crystal structure of CaV_2O_4 at room temperature contains two crystallographically inequivalent but similar V^{+3} $S = 1$ zigzag chains. These chains may therefore have different exchange constants associated with each of them. For simplicity, our $\chi(T)$ data were analyzed assuming a single type of zigzag chain. Furthermore, the extent to which the transitions at T_{S1} and T_S affect the magnetic interactions is not yet clear.

From crystal structure considerations, one expects that $J_2/J_1 \approx 1$ in CaV_2O_4 ,^{10,11} instead of $J_2/J_1 \approx 0$ as found here. This suggests that additional magnetic interactions and/or anisotropy terms beyond the Heisenberg interactions J_1 and J_2 and interchain coupling J_\perp considered here may be important. In addition to single ion anisotropy and other types of anisotropy, we mention as possibilities the Dzyaloshinskii-Moriya interaction, bi-quadratic exchange, and cyclic exchange interactions within the zigzag chains. When such additional terms are included in the analysis, the fitted value of J_2/J_1 could turn out to be closer to unity. A four-spin cyclic exchange interaction has been found to be important to the magnetic susceptibility in cuprate spin ladders.² In these spin ladders, there are exchange interactions J and J' between nearest-neighbor Cu^{+2} spins $1/2$ along the legs and across the rungs of the spin ladder, respectively. For the $S = 1/2$ two-leg ladder compound SrCu_2O_3 , if only J and J' are included in fits to the data, one obtains $J'/J \approx 0.5$.² However, by also including the theoretically derived cyclic four-spin exchange interaction, the ratio J'/J increases from 0.5 to a value closer to unity, as expected from the crystal structure.

Pieper *et al.* have recently proposed a very different and very interesting model to explain the inference that $J_2/J_1 \approx 0$ around room temperature which involves partial orbital ordering of the two d -electrons of V among the three t_{2g} orbitals.¹⁵ Furthermore, in order to explain the magnetic structure at low temperatures, they deduce that the nature of the orbital ordering changes below T_S such that the effective spin lattice becomes a spin-1 two-leg ladder.

It has been well documented that fits of magnetic susceptibility data by theory tests only the consistency of a spin model with the data, and not the uniqueness of the model. A good example of this fact arose in the study of the antiferromagnetic alternating exchange chain compound vanadyl pyrophosphate, $(\text{VO})_2\text{P}_2\text{O}_7$, the history of which is described in detail in the introduction of Ref. 51. The ultimate arbiter of the validity of a spin model is inelastic neutron scattering measurements of the magnetic excitation dispersion relations in single crystals. Theoretical calculations of the exchange interactions are much needed and would also be valuable in this regard.

Finally, the origin of the intrinsic heat capacity anomalies at $T_{S1} \approx 200$ K for the two *annealed* single crystals of CaV_2O_4 needs to be further studied. We speculate that this transition may be the long-sought chiral phase transition originally postulated by Villain in 1977.⁹

Note added—After this work and this paper were nearly completed, Sakurai reported a very interesting and detailed study of the magnetic and electronic phase diagram of polycrystalline samples of the solid solution $\text{Ca}_{1-x}\text{Na}_x\text{V}_2\text{O}_4$ prepared under high pressure.⁵²

Acknowledgments

We acknowledge useful discussions with R. McQueeney, and we thank D. Robinson for the excellent technical support of our high-energy x-ray diffraction study. Work at Ames Laboratory was supported by the United States Department of Energy-Basic Energy Sciences under Contract No. DE-AC02-07CH11358. Use of the Advanced Photon Source (APS) was supported by the U.S. Department of Energy, Office of Science, under Contract No. DE-AC02-06CH11357. The Midwest Universities Collaborative Access Team (MUCAT) sector at the APS is supported by the U.S. Department of Energy, Office of Science, through the Ames Laboratory under Contract No. DE-AC02-07CH11358. The work of A.H. was supported by the Deutsche Forschungsgemeinschaft through a Heisenberg fellowship and grant No. HO 2325/4-1. M.R. acknowledges fundings from Deutsche Forschungsgemeinschaft (grant UL 164/4).

* Present address: Department of Physics, Jamia Millia Islamia, New Delhi - 110025, India.

¹ D. C. Johnston, R. K. Kremer, M. Troyer, X. Wang, A.

- Klümper, S. L. Bud'ko, A. F. Panchula, and P. C. Canfield, *Phys. Rev. B* **61**, 9558 (2000).
- ² D. C. Johnston, M. Troyer, S. Miyahara, D. Lidsky, K. Ueda, M. Azuma, Z. Hiroi, M. Takano, M. Isobe, Y. Ueda, M. A. Korotin, V. I. Anisimov, A. V. Mahajan, and L. L. Miller, preprint arXiv:cond-mat/0001147 (2000).
- ³ E. Dagotto and T. M. Rice, *Science* **271**, 618 (2001).
- ⁴ M. Kaburagi, H. Kawamura, and T. Hikihara, *J. Phys. Soc. Jpn.* **68**, 3185 (1999).
- ⁵ T. Hikihara, M. Kaburagi, H. Kawamura, and T. Tonegawa, *J. Phys. Soc. Jpn.* **69**, 259 (2000).
- ⁶ T. Hikihara, M. Kaburagi, and H. Kawamura, *Phys. Rev. B* **63**, 174430 (2001).
- ⁷ A. K. Kolezhuk, *Phys. Rev. B* **62**, R6057 (2000).
- ⁸ For a recent theoretical review on 1D magnetism see H.-J. Mikeska and A. K. Kolezhuk, *Lect. Notes Phys.* **645**, Springer-Verlag, Berlin (2004), p. 1.
- ⁹ J. Villain, *Ann. Israel Phys. Soc.* **2**, 565 (1977).
- ¹⁰ H. Fukushima, H. Kikuchi, M. Chiba, Y. Fujii, Y. Yamamoto, and H. Hori, *Prog. Theor. Phys. Suppl.* **145**, 72 (2002).
- ¹¹ H. Kikuchi, M. Chiba, and T. Kubo, *Can. J. Phys.* **79**, 1551 (2001).
- ¹² B. F. Decker and J. S. Kasper, *Acta Cryst.* **10**, 332 (1957).
- ¹³ J. M. Hastings, L. M. Corliss, W. Kunmann, and S. La Placa, *J. Phys. Chem. Solids* **28**, 1089 (1967).
- ¹⁴ X. Zong, B. J. Suh, A. Niazi, J. Q. Yan, D. L. Schlagel, T. A. Lograsso, and D. C. Johnston, *Phys. Rev. B* **77**, 014412 (2008).
- ¹⁵ O. Pieper, B. Lake, A. Daoud-Aladine, M. Reehuis, K. Prokes, B. Klamke, K. Kiefer, J. Q. Yan, A. Niazi, D. C. Johnston, and A. Honecker, arXiv:0812.1808 (2008).
- ¹⁶ Y. Q. Yan, M. Reehuis, O. Pieper, B. Lake, A. Daoud-Aladine, Y. Mudryk, V. Pecharsky, Y. Ren, J. Fieramosca, A. Kreyssig, S. Das, A. Niazi, D. C. Johnston, R. J. McQueeney, P. Pattison, and E. Herman (unpublished).
- ¹⁷ O. Pieper, B. Lake, M. Enderle, T. G. Perring, A. Daoud-Aladine, J. Q. Yan, A. Niazi, and D. C. Johnston (unpublished).
- ¹⁸ Crystals were grown in the Materials Preparation Center, Ames Laboratory-USDOE, Ames, IA, USA. See <www.mpc.ameslab.gov>.
- ¹⁹ Rietveld analysis program DBWS-9807a release 27.02.99, ©1998 by R. A. Young, an upgrade of "DBWS-9411 - an upgrade of the DBWS programs for Rietveld Refinement with PC and mainframe computers, R. A. Young, *J. Appl. Cryst.* **28**, 366 (1995)".
- ²⁰ A. Kreyssig, S. Chang, Y. Janssen, J. W. Kim, S. Nandi, J. Q. Yan, L. Tan, R. J. McQueeney, P. C. Canfield, and A. I. Goldman, *Phys. Rev. B* **76**, 054421 (2007).
- ²¹ D. B. McWhan and J. P. Remeika, *Phys. Rev. B* **2**, 3734 (1970).
- ²² For a review, see J. M. Honig and L. L. Van Zandt, *Annu. Rev. Mater. Sci.* **5**, 225 (1975).
- ²³ H. V. Keer, D. L. Dickerson, H. Kuwamoto, H. L. C. Barros, and J. M. Honig, *J. Solid State Chem.* **19**, 95 (1976).
- ²⁴ W. Bao, C. Broholm, G. Aeppli, S. A. Carter, P. Dai, T. F. Rosenbaum, J. M. Honig, P. Metcalf, and S. F. Trevino, *Phys. Rev. B* **58**, 12727 (1998).
- ²⁵ S. Yonezawa, Y. Muraoka, Y. Ueda, and Z. Hiroi, *Solid State Commun.* **129**, 245 (2004).
- ²⁶ L. L. Miller, *Rev. Sci. Instrum.* **67**, 3201 (1996).
- ²⁷ P. Stamenov and J. M. D. Coey, *Rev. Sci. Instrum.* **77**, 015106 (2006).
- ²⁸ J. R. Carter and R. S. Feigelson, *J. Am. Ceram. Soc.* **47**, 141 (1964).
- ²⁹ J. S. Smart, *Effective Field Theories of Magnetism* (W. B. Saunders Company, Philadelphia, 1966).
- ³⁰ G. M. Schmiedeshoff, A. W. Lounsbury, D. J. Luna, S. J. Tracy, A. J. Schramm, S. W. Tozer, V. F. Correa, S. T. Hannahs, T. P. Murphy, E. C. Palm, A. H. Lacerda, S. L. Budko, P. C. Canfield, J. L. Smith, J. C. Lashley, and J. C. Cooley, *Rev. Sci. Instrum.* **77**, 123907 (2006).
- ³¹ R. M. Moon, *Phys. Rev. Lett.* **25**, 527 (1970).
- ³² A. Menth and J. P. Remeika, *Phys. Rev. B* **2**, 3756 (1970).
- ³³ S. A. Shivashankar and J. M. Honig, *Phys. Rev. B* **28**, 5695 (1983).
- ³⁴ S. A. Carter, T. F. Rosenbaum, M. Lu, H. M. Jaeger, P. Metcalf, J. M. Honig, and J. Spalek, *Phys. Rev. B* **49**, 7898 (1994).
- ³⁵ M. Troyer, B. Ammon and E. Heeb, *Lecture Notes in Computer Science* **1505**, 191 (1998); A. F. Albuquerque, F. Alet, P. Corboz, P. Dayal, A. Feiguin, S. Fuchs, L. Gamper, E. Gull, S. Gürtler, A. Honecker, R. Igarashi, M. Körner, A. Kozhevnikov, A. Läuchli, S. R. Manmana, M. Matsumoto, I. P. McCulloch, F. Michel, R. M. Noack, G. Pawłowski, L. Pollet, T. Pruschke, U. Schollwöck, S. Todo, S. Trebst, M. Troyer, P. Werner, and S. Wessel, *The ALPS Project Release 1.3: Open Source Software for Strongly Correlated Systems*, *J. Magn. Magn. Mater.* **310**, 1187 (2007); F. Alet, S. Wessel, and M. Troyer, *Phys. Rev. E* **71**, 036706 (2005); see also <<http://alps.comp-phys.org>>.
- ³⁶ O. F. Syljuåsen and A. W. Sandvik, *Phys. Rev. E* **66**, 046701 (2002).
- ³⁷ A. Kolezhuk, R. Roth, and U. Schollwöck, *Phys. Rev. Lett.* **77**, 5142 (1996).
- ³⁸ F. D. M. Haldane, *Phys. Rev. Lett.* **50**, 1153 (1983); F. D. M. Haldane, *Phys. Lett. A* **93**, 464 (1983).
- ³⁹ T. Xiang, *Phys. Rev. B* **58**, 9142 (1998).
- ⁴⁰ A. E. Feiguin and S. R. White, *Phys. Rev. B* **72**, 220401(R) (2005).
- ⁴¹ L. J. de Jongh and A. R. Miedema, *Adv. Phys.* **50**, 947 (2001).
- ⁴² B. Pedrini, J. L. Gavilano, D. Rau, H. R. Ott, S. M. Kazakov, J. Karpinski, and S. Wessel, *Phys. Rev. B* **70**, 024421 (2004).
- ⁴³ L. Shields, *J. Chem. Soc. (A)*, 303 (1970).
- ⁴⁴ J. Ashkin and N. S. Vandervan, *Physica B+C* **95**, 1 (1978).
- ⁴⁵ F. Kubec and Z. Sroubek, *J. Chem Phys.* **57**, 1660 (1972).
- ⁴⁶ E. D. Jones, *Phys. Rev.* **137**, A978 (1965).
- ⁴⁷ A. E. Feiguin, private communication (2008).
- ⁴⁸ O. Golinelli, Th. Jolicœur, and R. Lacaze, *Phys. Rev. B* **50**, 3037 (1994).
- ⁴⁹ S. R. White and D. A. Huse, *Phys. Rev. B* **48**, 3844 (1993).
- ⁵⁰ B. Pedrini, S. Wessel, J. L. Gavilano, H. R. Ott, S. M. Kazakov, and J. Karpinski, *Eur. Phys. J. B* **55**, 219 (2007).
- ⁵¹ D. C. Johnston, T. Saito, M. Azuma, M. Takano, T. Yamauchi, and Y. Ueda, *Phys. Rev. B* **64**, 134403 (2001).
- ⁵² H. Sakurai, *Phys. Rev. B* **78**, 094410 (2008).